This is a preprint, the final version is subject to change, of the American Mineralogist (MSA)
Cite as Authors (Year) Title. American Mineralogist, in press.
DOI: https://doi.org/10.2138/am-2020-6964

Revision 1

Microstructural controls on the chemical heterogeneity of cassiterite revealed by cathodoluminescence and elemental X-ray mapping

Jason M. Bennett[1], Anthony I. S. Kemp[1], Malcolm P. Roberts[2]

[1] Centre for Exploration Targeting, School of Earth Sciences, University of Western Australia

[2] Centre for Microscopy, Characterisation and Analysis, University of Western Australia

ABSTRACT

Quantitative X-ray element maps of cassiterite crystals from four localities show that Ti, Fe, Nb, Ta and W define oscillatory zonation patterns, and that the cathodoluminescent response is due to a complex interplay between Ti activated emission paired with quenching effects from Fe, Nb, Ta and W. Sector zonation is commonly highlighted by domains of high Fe, incorporated via a substitution mechanism independent of Nb and Ta. A second form of sector zonation is highlighted by distributions of W separate to the Fe-dominant sector zone. Both sector zones show quenched cathodoluminescence and are indistinguishable under routine SEM CL imaging. For cassiterite already high in Fe (and Nb or Ta), such as in pegmatitic or granitic samples, the internal structure of the grain may remain obscured when imaged by cathodoluminescence techniques, regardless of the presence of sector zonation. Careful petrogenetic assessments using a combination of panchromatic and hyperspectral CL, aided by quantitative elemental X-ray mapping, is a prerequisite step to elucidate cassiterite petrogenetic history and properly characterize these grains for in situ microanalysis. The absence of a clear petrogenetic

framework may lead to unknowingly poor spot selection during in situ analyses for geochronology and trace element geochemistry, and/or erroneous interpretations of U-Pb and O isotopic data.

Keywords: Cassiterite, Hyperspectral Cathodoluminescence, X-ray Element Mapping, Oscillatory Zonation, Sector Zonation

INTRODUCTION

Cassiterite (SnO_2) is the primary economic tin-bearing mineral recovered in a variety of polymetallic systems that include Li-Sn-Ta-(Nb) pegmatites such as the Greenbushes deposit, Western Australia (Partington et al. 1995), Sn-Cu-Pb-Zn skarns such as Gejiu, China (Cheng et al. 2013) and Sn-W hydrothermal vein and greisen systems such as Panasquiera, Portugal (Kelly and Rye 1979). It is also a common minor or accessory phase in other mineralized systems such as the In-bearing Pingüino epithermal polymetallic vein system in Argentina (Lopez et al. 2015), the Breves Cu-Au-(W-Bi-Sn) deposit in Brazil (Tallarico et al. 2004), and some intrusion-related Au systems (Thompson et al. 1999). This association of cassiterite with mineral systems enriched in the 'critical' metals W, Nb, Ta, Li and In (Chakhmouradian et al. 2015) makes this mineral a prime target for research, particularly into its development as a multi-process recorder of mineralizing processes.

Cassiterite is known to show complex growth structures including sector zonation, oscillatory zonation and microstructures that may reflect late stage hydrothermal overprinting (Hall and Ribbe 1971; Carr et al. 2017; Wille et al. 2018). A few recent studies have examined cassiterite as a U-Pb geochronometer using in situ analytical techniques, which requires characterization of the internal structure and growth history of each analyzed grain to provide the petrogenetic

framework for interpretation. Carr et al. (2017), Zhang et al. (2017), Guo et al. (2018), Neymark et al. (2018) and Cheng et al. (2019) used Scanning Electron Microscope (SEM) panchromatic cathodoluminescence (CL) to image the internal structure of their cassiterite crystals prior to U-Pb analysis. Unfortunately, only a few studies exist that aid in the interpretation of CL imaging of cassiterite for this purpose (Hall and Ribbe 1971; Farmer 1991; Wille et al. 2018).

In the present study, the chemical basis for zonation patterns in cassiterite is examined by incorporating panchromatic cathodoluminescence imaging and hyperspectral cathodoluminescence mapping with EPMA X-ray element mapping. With these analytical tools, the basis is provided for the interpretation of primary growth structures such as oscillatory and sector zonation, as well as microstructures that may reflect secondary processes like recrystallized (healed) fractures, post-crystallization diffusion fronts and dissolution-reprecipitation reactions. We find that sector zonation imparts a significant control on W and Fe uptake and distribution within cassiterite crystals, and that panchromatic CL imaging alone does not reveal the internal structure of cassiterite grains that have high Fe, Ta, Nb or W. Because of this, it is important that a combination of CL and quantitative elemental X-ray maps are acquired to properly characterize the microstructure and petrogenetic history of a cassiterite sample prior to in situ microanalysis.

BACKGROUND

Cassiterite crystallizes in the tetragonal system, class 4/mmm (Ditetragonal Dipyramidal), space group $P4_2/mnm$ and has unit cell parameters a = 4.7382(4) Å and c = 3.1871(1) Å (Bolzan et al. 1997). It is a member of the rutile structure group of $M^{4+}O_2$ oxides, which can be described by M^{4+} ions in six-fold coordination forming distorted octahedra joined along their shortest edges

into chains parallel to the c axis of the crystal. Rutile (TiO_2) is already in common use as a U-Pb geochronometer (Mezger et al. 1989) and as a geothermobarometer (Zack et al. 2004; Ferry and Watson 2007; Tomkins et al. 2007). As rutile is isostructural with cassiterite, it follows that cassiterite may also have use as a geochronometer or a geothermobarometer. The fact that cassiterite is a product of the primary mineralization process (barring secondary oxidation reactions of stannite, Cu_2FeSnS_4, or related minerals) means that the chemical and isotopic signatures preserved during crystal growth may be translated into a direct record of the physicochemical conditions of mineralization.

Cassiterite as a geochemical multi-tool

Underpinning the utility of cassiterite as a geochemical multi-tool, or the "zircon of mineralized systems" (Blevin and Norman 2010), is its application as a geochronometer. The use of Isotope Dilution Thermal Ionization Mass Spectrometry (ID-TIMS) for U-Pb dating in cassiterite was first attempted by Gulson and Jones (1992), however, the results were contentious (McNaughton et al. 1993). Due to the difficulties in achieving a thorough digestion of cassiterite (Clayton and Rojkovic 1999), U-Pb dating of cassiterite via ID-TIMS was not attempted again until Liu et al. (2007). To avoid the analytical hurdles associated with incomplete digestion of cassiterite, the last decade has seen a shift to in situ analytical methods for U-Pb geochronology, such as Laser Ablation Inductively Coupled Plasma Mass Spectrometry (LA-ICP-MS) and Secondary Ion Mass Spectrometry (SIMS) (Yuan et al. 2011; Zhang et al. 2013, 2014, 2017; Li et al. 2016; Carr et al. 2017; Deng et al. 2018; Guo et al. 2018; Moscati and Neymark 2019). Recently, the work of Carr et al. (2017) demonstrated that there are no orientation effects of U-Pb measurements on cassiterite when using SIMS, and Neymark et al. (2018) refined cassiterite LA-ICP-MS U-Pb dating methodology by claiming to remove the requirement of a matrix matched age standard.

The fundamental benefit of any in-situ analytical technique is the correlation between the measured chemical or isotopic data with paragenetic context and the ability to target discrete microstructural domains that formed at different stages of the growth history (including secondary processes). Currently, both the SIMS and LA-ICP-MS approaches to U-Pb dating of cassiterite rely upon the interpretation of internal microstructures revealed by CL techniques.

Cathodoluminescence in cassiterite

The chemical basis for CL response in cassiterite has been generally tied to a yellow 520-565 nm Ti activated emission and a blue 420-465 nm W activated emission (Hall and Ribbe 1971; Farmer 1991). While intrinsic cathodoluminescence has also been reported in nanocrystalline and thin-film SnO_2 studies from the materials science literature (Salviati et al. 2005; Korotcenkov et al. 2006; Maestre et al. 2007), the role of this activation mechanism has not been explored in natural systems. Hall and Ribbe (1971) suggest that Fe acts as a sensitizer for Ti emission up to a certain concentration threshold, after which Fe acts as a quenching agent. In contrast, Farmer (1991) suggests that Fe only exhibits quenching behavior. Farmer (1991) also notes CL quenching due to the presence of Fe with W, and Fe with Nb and Ta, in agreement with the observations of Hall and Ribbe (1971). While intrinsic luminescence may play a role in the CL response of natural cassiterite crystals and cannot be discounted, the strong correlation between chemistry and CL signature (Hall and Ribbe 1971; Farmer 1991) suggests that the microstructures observed via CL imaging techniques are dominantly due to the distribution and incorporation of minor components of Ti, Fe, Nb, Ta and W into the cassiterite lattice.

Minor element substitution mechanisms in cassiterite

Numerous possible substitution mechanisms for the incorporation of Ti, Fe, Mn, Nb, Ta and W in cassiterite exist. The incorporation of Ti^{4+} is generally agreed to be via direct substitution with Sn^{4+} (Izoret et al. 1985; Neiva 1996). This is presumably the same incorporation mechanism for Zr^{4+}, similar to the reactions invoked for the incorporation of Sn^{4+} and Hf^{4+} in rutile (Fromknecht et al. 1996). Homovalent substitution is also possible for Nb^{4+} and Ta^{4+}, which also crystallize as rutile-structured MO_2 oxides, but no evidence has been provided for their substitution in this manner. Instead, most studies suggest the incorporation of these elements in the pentavalent state (Izoret et al. 1985; Möller et al. 1988; Neiva 1996, 2008) via two potential coupled substitution reactions depending on the oxidation state of Fe. An Electron Paramagnetic Resonance (EPR) study on the oxidation state of Fe in cassiterite by Izoret et al. (1985) provides evidence for a 1:1 stoichiometry with Fe^{3+}:

$$(Ta,Nb)^{5+} + Fe^{3+} \rightleftharpoons 2Sn^{4+} \qquad \textbf{(1)}$$

A Mössbauer study focusing on the oxidation state of Fe in cassiterite (Möller et al. 1988) suggests a 2:1 stoichiometry of the style:

$$2(Ta,Nb)^{5+} + Fe^{2+} \rightleftharpoons 3Sn^{4+} \qquad \textbf{(2)}$$

From a geochemical perspective, most studies support the 2:1 mechanism of equation 2, which may represent a limited solid solution with the columbite group minerals. A minor component of equation 1 is usually described to account for an excess of Fe beyond the 2:1 stoichiometry (Neiva 1996, 2008).

An 'excess of Fe' may also be reconciled with Fe substitution reactions that do not involve Nb or Ta. Izoret et al. (1985) propose a reaction where Fe^{3+} occupies the normal six-fold coordination Sn^{4+} site, coupled with some Fe^{3+} that exists in a portion of interstitial sites to balance charge:

$$Fe^{3+} + \frac{1}{3}Fe_i^{3+} \rightleftharpoons Sn^{4+} + \square_i \quad \textbf{(3)}$$

In the samples of Izoret et al. (1985), a correlation exists between Ti and Fe, hinting at a mechanism where the existence of these interstitial sites in the cassiterite lattice are related to the incorporation of some Ti^{4+}. Izoret et al. (1985) argue that the ionic radius of Ti^{4+}, slightly smaller than Sn^{4+}, results in a volume contraction of the octahedral coordination polyhedron of the usual cation site, allowing for the opening of a nearby interstitial site large enough for the incorporation of an Fe^{3+} cation. The charge balance required for the direct substitution of Fe^{3+} may also be balanced by the addition of a H^+ ion on a nearby oxygen (Möller et al. 1988) via the equation:

$$Fe^{3+} + OH^- \rightleftharpoons Sn^{4+} + O^{2-} \quad \textbf{(4)}$$

This remains the favored reaction, as the coupling of Fe^{3+} with OH^- has been described through EPR studies (Dusausoy et al. 1988; Ruck et al. 1989) with the incorporation of hydroxyl groups into the rutile group lattice confirmed by Fourier-transform Infrared (FTIR) spectroscopy studies on cassiterite (Maldener et al. 2001; Losos and Beran 2004) and structurally described through neutron and X-ray diffraction studies on rutile (Swope et al. 1995). This reaction could also be described as the result of limited solid substitution with varlamoffite, an International Mineralogical Association (IMA) approved but 'questionable' species with the formula $(Sn,Fe)(O,OH)_2$ (Sharko 1971; Jambor et al. 1995).

Möller et al. (1988) also studied the substitution of W into the cassiterite lattice via three possible reactions:

$$W^{4+} \rightleftharpoons Sn^{4+} \quad \textbf{(5)}$$

153 $$W^{6+} + Fe^{2+} \rightleftharpoons 2Sn^{4+} \quad \textbf{(6)}$$

154 $$W^{6+} + 2Fe^{3+} \rightleftharpoons 3Sn^{4+} \quad \textbf{(7)}$$

155 Möller et al. (1988) discard the possibility of W^{4+} substitution due to the presence of Fe^{3+} in most
156 W-rich samples, and most of their data support the ferberite ($FeWO_4$) stoichiometry of equation
157 6.

158 Theoretically, Mn may play an important role in charge balance along with Fe in any of the
159 coupled substitution mechanisms described above, although in contrast to the other elements, the
160 incorporation mechanisms for Mn in cassiterite are comparatively poorly studied. Some analyses
161 for Mn in cassiterite are reported in studies on the columbite group minerals from pegmatites. In
162 general, the Mn contents of these samples tend to be low, with a preference for the
163 stoichiometries of tapiolite-(Fe) or tantalite-(Fe) observed for cassiterite when plotted in the
164 columbite-tantalite quadrilateral (Beurlen et al. 2007; Galliski et al. 2016; Yan et al. 2016);
165 however, Mn-dominant stoichiometries have also been previously described (Masau et al. 2000).

166 **Cathodoluminescent microstructures in cassiterite**

167 The variable CL response due to the interaction of the elements discussed above, and the variety
168 of independent and codependent substitution mechanisms for their incorporation into the
169 cassiterite lattice, results in a wide range of complex microstructures observed in cassiterite
170 under CL illumination. Primary microstructures, which arise during crystal growth, include
171 concentric zonation (e.g., oscillatory zonation) and sector zonation. Secondary microstructures
172 arise during subsequent modification of a crystal via fracture healing, diffusion, dissolution-
173 reprecipitation and annealing processes. While many authors have noted the existence of these

microstructures in their work on cassiterite, only a few studies characterize these features in any detail (Hall and Ribbe 1971; Carr et al. 2017; Wille et al. 2018).

Concentric zonation. Concentric zonation is a commonly observed microstructure defined by variations in crystal chemistry parallel to crystallographic growth planes and has long been recognised as a potential record of the dynamic environment of crystal growth (e.g., Frondel et al. 1942). The chemical variation is usually in the ratio of end-member components of solid solution series, for example in the albite-anorthite (Vance 1962) and grossular-andradite systems (Jamtveit 1991). These systems have been the focus for the cause of oscillatory zonation, a microstructure where the compositional change repetitively switches between these end members (Ortoleva 1990; Shore and Fowler 1996), commonly displaying self-affine fractal behavior (Halden and Hawthorne 1993; Holten et al. 1997).

Despite the wide recognition of oscillatory zonation in cassiterite (Hall and Ribbe 1971; Farmer 1991; Carr et al. 2017; Wille et al. 2018), there are no detailed models for the development of this feature. Nevertheless, comparisons can be made with existing models in the literature for other minerals. Oscillatory zonation may reflect changes in the physicochemical properties of the growth medium (Yardley et al. 1991; Jamtveit and Hervig 1994), in the case of cassiterite this medium may be a silicate magma or an aqueous fluid. Oscillatory zonation may also reflect changes in rate dependent non-linear thermodynamic properties of the system (Ortoleva 1990; Reeder et al. 1990; Holten et al. 2000), as equilibrium between cassiterite and the bulk medium may not be attained. Hydrothermal-metasomatic cassiterite is undoubtedly a result of open-system processes, and mass transport and flux through these systems (Jamtveit 1991; Putnis et al. 1992; Jamtveit et al. 1995; L'Heureux and Jamtveit 2002) is likely to play a large role on local cassiterite-fluid equilibria.

As oscillatory zonation may be a non-equilibrium feature, attribution of oscillatory zonation in a sample to either a closed or open system, or equilibrium or disequilibrium processes, is vital for the interpretation of in situ trace element and isotopic data obtained from such domains. It is also important to note that while all oscillatory zonation is a concentric growth zonation, not all concentric growth zonations are oscillatory. In this work, we reserve the term 'oscillatory zonation' as a distinct subset of concentric growth zonation to refer to any concentric growth patterns that show signs of periodicity, regardless of scale. We also reserve the term 'growth domains' to refer to broader aperiodic concentric growth zones that show marked changes in chemistry, color, or CL response, and which may or may not contain 'oscillatory zonation' as a feature of that specific 'growth domain'.

Sector zonation. Sector zonation has been described in cassiterite (Farmer 1991) following the protosite model of Nakamura (1973) and Dowty (1976). In cassiterite, the Sn^{4+} ions sit in 6-fold (octahedral) coordination. At the growth face, new Sn^{4+} ions adsorb onto partially coordinated sites (protosites) with only a fraction of the full 6-fold coordination. Farmer (1991) calculated the protosite coordination for each of the major growth forms of cassiterite; the {100} and {101} forms exhibit 3/6 coordination, the {111} form 3.5/6 coordination, the {001} form 4/6 coordination and the {110} form 4.5/6 coordination. Dowty (1976) suggested that protosites closer to full coordination (such as the {110} form of cassiterite) are less likely to retain impurities, whereas more open protosites with lower coordination (such as the {100} form of cassiterite) are more likely to retain impurities.

Farmer (1991) commented on two different behaviors of {101} sectors related to their relative W and Fe contents across two paragenetic stages, but made no further comments on the chemical

contents of other sectors. To date, no other study has reported chemical preferences between different growth faces in cassiterite.

Secondary processes. Post-primary modification processes have been noted in cassiterite via cross cutting relationships of certain CL features (Hall and Ribbe 1971; Carr et al. 2017; Wille et al. 2018). Similar features have been seen in other minerals and may serve as a first order comparison with cassiterite. For instance, the rates of diffusion of Pb and Zr in isostructural rutile are well described (Cherniak and Watson 2001; Cherniak et al. 2007) and the physical and chemical basis for dissolution-precipitation processes in zircon (Geisler et al. 2001, 2002, 2003, 2007) and alkali-halide salts (Glynn and Reardon 1990; Putnis and Mezger 2004; Pollok et al. 2011; Ruiz-Agudo et al. 2014) are well studied. The process of fracture healing in quartz is also well documented (Smith and Evans 1984; Brantley et al. 1990). The chemical basis of these features is yet to be described in cassiterite, and current understanding is based on morphological characteristics only.

CL-dark crystals. Cassiterite crystals are also known to show no CL response under certain circumstances, most notably those crystals reportedly high in Fe (Farmer 1991). Farmer (1991) notes that these crystals are commonly sourced from pegmatites, although others have reported CL non-responsive crystals from other styles of mineralization (Carr et al. 2017; Neymark et al. 2018; Cheng et al. 2019). As these crystals offer little information under CL illumination, their internal chemical variability (and any microstructures hidden within) remain poorly studied.

METHODS

Sample Selection and Description

Candidate grains were screened for the presence of microstructures listed in Table 1 and ultimately selected to represent a range of mineralization styles. Seven crystals were selected from four localities: two crystals are from the Mount Bischoff cassiterite-sulfide skarn (MB1 and MB2), two are from the alluvial (hydrothermal greisen/vein) Saltwater Creek deposit (SC1 and SC2), two from the greisen zone of the Buriti mine (BM1 and BM2) and one is from the White Lode Sn-mineralized granite (WL1). A locality summary is presented in Table 2, including approximate coordinates for these deposits.

Mount Bischoff is a pyrrhotite-cassiterite skarn located in northwestern Tasmania, Australia. Tin mineralization is interpreted to have occurred in the retrogressive stages of a high temperature Mg-skarn. The skarn borders porphyritic dikes which have been interpreted to act as a conduit for fluid flow, rather than the source of the mineralizing fluids (Halley and Walshe 1995).

The studied hand sample from Mount Bischoff consists of approximately 80% cassiterite, 10% sellaite (MgF_2), 8% quartz, and trace pyrrhotite and chalcopyrite. There are minor amounts of clay and carbonate minerals infilling voids (2-3 mm in size) between cassiterite, quartz and sellaite.

In a thin section prepared from this sample, the cassiterite exists predominantly as subhedral groundmass, <0.5 mm in size, intergrown with sellaite and quartz. The quartz is usually euhedral, 1-2 mm in size, and lines the 2-3 mm voids along with euhedral cassiterite crystals that are up to 1 mm. The sellaite tends to be euhedral to subidiomorphic and is mostly intergrown with subhedral cassiterite in the groundmass.

Two crystals (MB1 and MB2) were chosen for hyperspectral CL and X-ray element mapping after a reconnaissance survey in transmitted plane polarized light, selected for being the largest euhedral crystals sectioned close to perpendicular to the c-axis.

Saltwater Creek is an alluvial tin locality near Coles Bay on the Freycinet Peninsula on the eastern coast of Tasmania. Cassiterite occurs as placer deposits along the creek, historically mined as the Schouten Main deposits (Twelvetrees 1901) and L.D. McRae's Workings (Keid 1951). The primary mineralization is interpreted as subeconomic greisenized granite and quartz-cassiterite veins, which have been observed locally in outcrop (Twelvetrees 1901).

The cassiterite crystals from Saltwater Creek analyzed in this study were supplied as a heavy mineral separate panned directly from the creek. The crystals are sub-angular, average around 0.5 mm in size with a few crystals near 1 mm diameter. Several crystals were mounted in a 2.54 cm epoxy disk, and two were selected for hyperspectral CL and X-ray element mapping after reconnaissance via panchromatic SEM CL imaging.

The Buriti tin mine is described as localized greisen mineralization overprinting a more laterally expansive Na-metasomatized granite (described as a hydrothermal albitite) developed on the margin of the Serra Dourada granite massif, located in the Goiás Tin Province of Brazil (Botelho and Moura 1998; Lenharo et al. 2002).

The cassiterite crystals examined from this locality were supplied as a heavy mineral separate. Several crystals were identified and hand-picked under a stereomicroscope and mounted in a 2.54 cm epoxy disk. As with the samples from Saltwater Creek, two crystals were selected for further analysis after reconnaissance CL imaging.

The White Lode is a mineralized granite occurrence at Poona, near Cue in the northwestern Yilgarn Craton of Western Australia. Poona is known for its emeralds and alexandrites at the adjacent Aga Khan mine (Grundmann and Morteani 1998; Marshall et al. 2016). Less well known are two occurrences of Sn-mineralization nearby, the White Lode and the Poona Tinshaft, a small Sn-Ta-Nb-pegmatite. The cassiterite crystals examined in this study originate from the White Lode and are hosted in a matrix that is heavily kaolinized (hence the name 'White Lode') and now consists of kaolinite-quartz-cassiterite. The textures seen in the kaolinized samples from the White Lode suggest that the original rock was a coarse-grained granite, rather than a pegmatite, as crystal sizes are no greater than 1 cm.

The cassiterite crystals from White Lode were extracted by crushing the friable host material, and several small 1-2 mm diameter crystals were hand-picked and mounted in a 2.54 cm epoxy disk. The most euhedral crystal (least damaged during crushing) was selected for hyperspectral CL and X-ray element mapping.

Optical and Cathodoluminescence Imagery

All samples were examined optically under polarized reflected light to assess optical continuity and to identify twin planes and grain boundaries where present. The cassiterite crystals from Mount Bischoff were also examined in transmitted light to assess their optical coloration. Panchromatic SEM CL images were obtained with the Tescan Vega3 SEM at the Centre for Microscopy, Characterisation and Analysis (CMCA) at the University of Western Australia (UWA).

Hyperspectral Cathodoluminescence

Hyperspectral cathodoluminescence maps were collected with the JEOL JXA-8530F Hyperprobe, also housed at the CMCA. Operating conditions were a 40 nA and 20 kV beam with a 100 ms dwell time for each 2 x 2 μm pixel. The hyperspectral data were acquired using the xCLent software package developed by CSIRO ("xCLent-Image v3.1.30.0" 2013) and false-color images were generated off-line by assigning the bandwidths 200-500 nm to the blue channel, 500-600 nm to the green channel, and 600-900 nm to the red channel. All hyperspectral maps were collected prior to quantitative X-ray element mapping. Attempts at hyperspectral CL map acquisition after X-ray element mapping achieved poorer results, presumably due to interaction effects between the electron beam and the cassiterite lattice.

Quantitative X-ray Element Maps

Quantitative X-ray element maps were also collected with the JEOL JXA-8530F Hyperprobe with a fully focused electron beam and the same analytical conditions as the hyperspectral CL map acquisition. Calibrations were performed with the standards as listed in Table 3. The quantitative maps were processed using Probe for EPMA® and CalcImage® software packages (Donovan 2018). The calibrated maps were then exported to Golden Software's Surfer® where the scales were adjusted for each element to cover the same range (0 to 0.6 at%) allowing for a direct comparison between samples. This also results in comparable detection limits, so that all elements show a limit of detection around 0.05 to 0.1 at%. The color scale was adjusted so that the black to dark blue transition marks this region, with all colors above light blue well above the detection limit. The scale for Sn was adjusted to span from 31.33 at% to the stoichiometric limit of 33.33 at% (i.e., 94 to 100 mol% SnO_2).

RESULTS

The descriptions below refer to optical, CL and X-ray elemental maps of the different cassiterite grains of this study, shown in Figures 1 to 12. In detail, these images show an array of complex features and structures. For brevity and clarity of description, specific features are arrowed in lower case letters on the figures, and these are referred to below, prefixed by the figure number (e.g., Figure 1a refers to the feature labeled 'a' in Figure 1, etc.).

Mount Bischoff

In plane polarized transmitted light, crystal MB1 from Mount Bischoff exhibits non-pleochroic colorless, light brown, and dark brown concentric growth domains (Figure 1a-d). The inner colorless domain (Figure 1b) is represented by fine scale oscillatory zonation in the panchromatic CL image (Figure 2a). The central light brown domain (Figure 1a) also shows weak oscillatory character, which is best observed in the hyperspectral CL map (Figure 2b). The dark brown domain of the crystal (Figure 1c) does not show fine scale oscillatory zonation in CL and correlates with the highest Fe concentrations between 0.35 and 0.55 at% (Figure 3a). The optically darkest sectors of the crystal (Figure 1e, f) correlate with sector zones of high W contents up to 0.5 at% (Figure 3b, c) and Fe concentrations below detection (Figure 3d, e).

The oscillatory CL response (Figure 2a) is mirrored by the Ti and Fe X-ray element maps (Figure 3f, g), with the CL-bright bands corresponding to Ti contents of around 0.2 at% and Fe concentrations below the detection limit (<0.5 at%). This is also seen in crystal MB2 (Figure 2c, d and Figure 4a, b). However, Ti concentrations 0.4 at% or higher (such as the bands indicated in Figures 3h and 4c) do not result in a CL-bright response (Figure 2e, f) even when also matched with Fe below the detection limit (Figures 3i and 4d).

In both MB1 and MB2, the high W sector zones range from 0.1 to 0.5 at% W (Figures 3b, c and 4e), are coupled with Fe concentrations that range from below the detection limit to around 0.25 at% (Figures 3d, e and 4f) and correlate with the dark blue sectors in the hyperspectral CL maps (Figure 2g, h, i). The CL-bright bands with the most vivid blue response in the false-colored hyperspectral CL maps (such as those indicated at the tip of the arrow in Figure 2i) are observed locally within the W-rich sectors where a concentric growth domain results in W below the detection limit (Figure 4g) coincident with Ti in moderate concentrations of around 0.2 at% (Figure 4h).

In MB2, a second form of sector zonation is clearly distinguishable as the red sectors in the false-colored hyperspectral CL map (Figure 2j) which matches regions where the Fe concentrations are below 0.2 at% (Figure 4i) with no detectable W (Figure 4j). Irregular CL-bright cross cutting features (e.g., Figure 2k) correspond with a decrease in Fe concentrations from around 0.5 at% to below the detection limit (Figure 3j). There appears to be no corresponding change in the other minor elements, although these were already below detection in this area.

Under plane polarized reflected light, the moderate bireflectance of cassiterite is apparent between grain boundaries and twin planes (Figure 1, dashed lines). Twin planes are not seen in the CL images, except for where they form boundaries with either form of sector zonation. Niobium, Ta, Zr and Mn are all below the detection limit for these two crystals (Figures 3 and 4).

Saltwater Creek

The Saltwater Creek crystals show contrasting CL dark and bright sectors in both the panchromatic and hyperspectral CL maps. In SC1, the main contrasting feature is a CL-bright oscillatory zoned sector (Figure 5a) and a homogenous CL-dark sector zone (Figure 5b) that

367 correlates very well with the element map for W (Figure 6a, b). The oscillatory bands in the CL-
368 bright zone parallel the growth zones highlighted by the Ti map (Figure 6). As with the Mount
369 Bischoff sample, individual bands with Ti concentrations greater than 0.4 at% (Figure 6c) also
370 correlate with a CL-dark response (band indicated in Figure 5c). This band also correlates with
371 Nb concentrations just above the limit of detection, being slightly over 0.1 at% (Figure 6d). The
372 Nb contents are noticeably higher in the CL-dark sector zone (Figure 6e), where the Fe contents
373 are mostly below the detection limit (Figure 6f). Fe is higher in the CL-bright side of the crystal
374 (Figure 6g) where concentrations approach 0.15 at%, although this sample is comparatively Fe
375 poor. There are no detectable contents of Ta, Zr or Mn for this sample.

376 Cassiterite SC2 contains similar contrasting CL-bright (Figure 5d) and CL-dark (Figure 5e)
377 sectors that can be seen in the panchromatic CL image. The CL-bright sector of the crystal is
378 characterized by moderate Fe contents, mostly around 0.3 at% (Figure 7a), with Ti, Nb and W
379 contents below the detection limit. The CL-dark sector of the crystal displays primary growth
380 bands that contain W contents up to 0.35 at% (Figure 7b) with Nb (Figure 7c) and Ti (Figure 7d)
381 concentrations up to 0.2 at%. The concentration of Fe on this side of the crystal is just above the
382 detection limit, near 0.15 at% (Figure 7e).

383 In addition, the CL-dark sector is cross-cut by a network of irregular CL-bright features (Figure
384 5f), which internally show convolute detail. In the hyperspectral CL map, two generations of
385 these CL-bright features can be distinguished based on their overall orientation and luminescence
386 character; a generation with a subvertical orientation (Figure 5g), and a generation with a
387 brighter CL response which appears to be cross cutting the previous generation in a
388 subhorizontal orientation (Figure 5h, red arrows indicate orientation direction). These irregular
389 CL features are most prominent in the left half of the crystal, mostly bound by a twin plane

(indicated by the dashed line in Figure 5i), although a lower CL responsive cross-cutting feature (Figure 5j) occurs on the right side of the crystal.

Regardless of the subtle intensity difference of the CL response in the hyperspectral maps, these irregular networks show the same chemical characteristics in the X-ray element maps, with Ti contents around 0.2 at% (Figure 7f) and Fe, Nb and W contents below the detection limit (Figure 7g-i). Tantalum, Zr, and Mn are all below the detection limit in this crystal.

Buriti Mine

Crystal BM1 shows fine scale oscillatory zonation (Figure 8a), CL-dark sector zonation (Figure 8b) and a mottled CL-bright cross-cutting feature extending from the rim of the crystal (Figure 8c). In the X-ray element maps, the cross-cutting feature displays an overall increase in Ti to around 0.3 at% (Figure 9a), while the Nb (Figure 9b) contents are depleted to below the detection limit relative to the initial concentrations in the host crystal. Tungsten and Fe show no variation associated with this feature (Figure 9c, d), however the concentration of these elements is in general below the detection limit for much of the crystal. The fine scale oscillatory zonation (Figure 8a) broadly correlates with the concentric banding in Ti (Figure 9e) and Nb (Figure 9f). The concentration of Zr is just above the detection limit in this crystal, and shows weak concentric banding (Figure 9g), but most noticeably Zr is also depleted in the CL-bright cross-cutting feature (Figure 9h). Some iron oxide inclusions are also present, localized within the cross-cutting feature (Figure 9i). Smaller cross-cutting features are also seen throughout the crystal (Figure 8d), and Mn and Ta are both below the limit of detection.

Under the same contrast and brightness settings used for panchromatic CL imaging of BM1, cassiterite sample BM2 was uniformly dark and generally uninterpretable. Adjusting the

brightness and contrast to maximum allowed for the discrimination of some subtle patchy textures (Figure 8e, f) associated with inclusions of fluorite (Fl) and columbite group minerals (CGM) which appear as small CL-bright inclusions.

More detail can be discerned from the hyperspectral map, which shows three regions that are entirely CL-dark (Figures 8g-i), a region which has a blue hue (Figure 8j), and a region with a subtle red-pink hue (Figure 8k). The remainder of the crystal displays weak oscillatory zoning (Figure 8l) overprinted by a CL-bright rim (Figure 8m) and numerous cross-cutting features (Figure 8n).

The X-ray element maps for BM2 show further complexity, with W concentrations of 0.15 at% (Figures 10a-c) that correlate with the hyperspectral blue region (Figure 8j) and two of the CL-dark regions (Figures 8g, h) but not the third dark region (Figure 8i). Instead, this last CL-dark region is associated with Nb contents that are around 0.15 at% (Figure 10d). Iron concentrations reach up to 0.15 at% in all of these regions (Figure 10e-h) but is below detection in the remainder of the crystal. The red-pink region (Figure 8k) correlates with Nb contents just above the detection limit (Figure 10i) and moderate Ti concentrations around 0.25 at% (Figure 10j).

The CL-bright outer zone (Figure 8m) also correlates with Ti contents around 0.25 at% (Figure 10k), as do the numerous cross-cutting features (Figures 8n and 10l). The weak oscillatory zonation visible in the hyperspectral map (Figure 8l) cannot be observed in the X-ray element maps. Tantalum, Zr and Mn are below the limit of detection in this crystal.

White Lode

Cassiterite crystal WL1 shows optical continuity under cross polarized reflected light, with no obvious twin planes or boundaries between cassiterite crystals of different orientations. There are

434 numerous randomly oriented inclusions of quartz and albite, with a trace of K-feldspar and Nb-
435 Ta oxides.

436 Panchromatic CL imagery of crystal WL1 was obtained through over exposure by maximizing
437 both brightness and contrast, similar to the conditions required to image BM2. The resulting
438 image reveals only minor CL-bright cross-cutting features (Figure 11a) and a faint mottled zone
439 (Figure 11b). Hyperspectral CL mapping resolves the cross-cutting features in finer detail
440 (Figure 11c), along with enhanced visibility of the mottled zones, which have a pink hue (Figure
441 11d), but the rest of the crystal remains CL-dark (Figure 11e).

442 The quantitative X-ray maps for WL1 (Figure 12) reveal complicated structural detail obscured
443 within both the panchromatic and hyperspectral CL maps. The Sn X-ray element map highlights
444 two distinct chemical regions of the crystal: region A with 32.5 – 33 at% Sn (Figure 12A, all of
445 the yellow-orange regions in the Sn X-ray element map) and a growth zoned region B with 31.7
446 – 32.5 at% Sn (Figure 12B, all of the green-blue regions in the Sn X-ray element map). These
447 two regions are distinguished by a clear dichotomy in their Fe-Nb-Ta contents; region A
448 corresponds to concentrations less than 0.15 at%, while region B corresponds to moderate to
449 high concentrations of Fe (0.3 – 0.6 at%), Nb (0.15-0.35 at%) and Ta (0.3 – 0.5 at%).

450 Most of region A corresponds to CL-bright cross-cutting and mottled features detected under
451 hyperspectral CL. For instance, the cross-cutting feature (Figure 11c) and the mottled feature
452 (11d) correspond to a high concentration of Sn (Figure 12c, d), low Ti (Figure 12e, f) and Fe
453 (Figure 12g, h), Nb (Figure 12i, j) and Ta (Figure 12k, l) concentrations below the detection
454 limit. However, some parts of region A have similar concentrations of Fe, Ti, Nb and Ta as the

455 CL mottled features (for example, Figure 12m), but they have no associated CL signature (Figure
456 11f). Tungsten, Zr and Mn are all below the detection limit in this crystal.

457 **DISCUSSION**

458 **Cathodoluminescence**

459 Comparison of the X-ray element maps (e.g., Figure 3) with the hyperspectral CL maps (e.g.,
460 Figure 2) show that Ti correlates well with the CL response, as would be expected for the 565
461 nm Ti-activated emission reported by Hall and Ribbe (1971). In detail, certain discrepancies are
462 noticeable. For instance, bands of high Ti (e.g., Figure 3h) that correspond with low contents of
463 other elements are CL-dark (Figure 2e), suggesting that Ti, with a concentration threshold near
464 0.4 at%, exhibits self-quenching (or concentration-quenching) behavior (Nasdala 2003).

465 Hall and Ribbe (1971) also note that the presence of Fe with Ti has the effect of enhancing the Ti
466 emission, although the data presented here suggest the opposite. For example, in Figure 4i, where
467 the Fe content is decreased in the sector zone but the Ti concentration remains constant parallel
468 to the oscillatory growth zonation, the CL-response is brighter (Figure 2j). In fact, comparison of
469 the CL-dark regions with areas of high Fe contents suggests that Fe only acts to inhibit
470 cathodoluminescence in cassiterite, in line with similar observations from Farmer (1991)

471 The regions of cassiterite that contain high W concentrations correspond to the CL-dark sector
472 zones, pointing to action of W as a CL quenching agent. This observation is inconsistent with the
473 reported blue 440 nm W activated emission of Hall and Ribbe (1971). While these authors report
474 quenching due to a combination of Fe and W, the X-ray element maps show that the W-rich
475 zones are also low Fe. In the false-colored hyperspectral maps, some regions of the CL-dark
476 sector zones do display a blue hue (e.g., Figure 2i) – these regions correlate with low W (<0.1

at%) and moderate Ti (0.2 at%) concentrations implying that the blue emission may be due to a coupled W and Ti mechanism. This agrees with the observations of Hall and Ribbe (1971), as the W concentrations reported in their analyses are at lower levels than observed here within the W-rich sector zones, and Ti is also present in their samples. Hall and Ribbe (1971) did not report measurements from their CL-dark sector zones for comparison, which may have also been high-W sector zones, but they do describe CL quenching due to the incorporation of Nb and Ta, in agreement with our CL-dark high Nb and Ta samples.

Our observations suggest that Ti is the sole extrinsic CL activator in cassiterite, up to a threshold near 0.4 at%. The presence of Fe, Nb, Ta or W all act to inhibit any CL response, but at low concentrations (<0.1 at%) they have the potential to shift the spectral response of the Ti-activated CL emission. This results in subtle differences in the hue of the CL response within and across cassiterite crystals, as detected in our work via hyperspectral CL, and reported previously in optical CL imagery (Hall and Ribbe 1971; Farmer 1991).

Concentric Growth Zonation

A. Hydrothermal-Metasomatic Systems. The two mapped crystals from the Mount Bischoff sample (Figures 3 and 4) show correlating patterns in their concentric growth domains detected optically via transmitted light, and via CL and X-ray mapping techniques. The correlating step changes in chemistry, repeatedly discernable within multiple crystals, suggest that cassiterite from Mount Bischoff provides a record of changing fluid chemistry in the system, similar to observations of other minerals from hydrothermal-metasomatic environments (Yardley et al. 1991). This implies an extrinsic mechanism for the high Ti cores (Figure 3h) of these cassiterite crystals, and thus may be a reflection of the activity of F and Cl in this system, as Ti is known to

499 be highly mobile in F and Cl-rich aqueous fluids under upper crustal conditions (Rapp et al.
500 2010). High F and Cl activities are expected in Sn-mineralizing systems, and at Mount Bischoff
501 in particular, the cores of these cassiterite crystals commonly contain sellaite (MgF_2).

502 While the large domain-scale zonation in Ti seems likely a record of deposit-scale fluctuations in
503 fluid chemistry, the finer scale oscillations need not be limited to extrinsic variables. However, it
504 is interesting to note that the same pattern of oscillatory bands occurs across both mapped
505 cassiterite grains (e.g., Figure 3f, 4a), implying that the oscillations are the result of local short-
506 range equilibrium of extrinsic variables, at least across distances up to 2 cm (the separation
507 distance between the crystals observed). Alternatively, synchronization of intrinsic variables due
508 to external noise (Holten et al. 2000) may explain this behavior, without the requirement of local
509 equilibrium.

510 As the samples from both Saltwater Creek and the Buriti mine were provided as loose cassiterite
511 crystals extracted from heavy mineral concentrates, any information pertaining to associated
512 mineralogy and relative timing is lost, and a comparison of the zonation patterns between
513 synchronous growth domains and cogenetic phases cannot be made. Regardless, the general
514 chemical characteristics of the oscillatory zonations are similar for cassiterite grains from these
515 two localities. In SC1, SC2 and BM1, strong oscillatory zonation can be seen in Ti, similar to the
516 oscillatory zonation seen in the cores of the Mount Bischoff cassiterite. In crystal BM2, the
517 oscillatory zonation in Ti is comparatively weak but observable in the hyperspectral image
518 (Figure 8l). The presence of oscillatory Ti zonation across these three localities suggests that this
519 may be diagnostic for cassiterite crystals of hydrothermal-metasomatic origin.

Since the incorporation mechanism for Zr and Ti into the cassiterite lattice is via direct homovalent substitution, it might be expected that the distribution of Zr within a cassiterite crystal should reflect the distribution of Ti. The strong oscillatory nature of Ti is not observed in the Zr X-ray element maps, as Zr is mostly below the limit of detection. However, when weak zoning is observed, at concentrations just above the detection limit (e.g., Figure 9g, h), the distribution of Zr does not match the observed variation in Ti distribution. This is likely due to the solubility mechanism of Zr in upper crustal hydrothermal systems, where Zr is transported via silica complexation in Si-rich fluids, and is thus sensitive to the concentration of Si in the fluid (Ayers et al. 2012). The activity of Si in Sn-mineralized hydrothermal-metasomatic systems would likely be buffered due to the ubiquity of quartz. This would in turn provide a buffer against fluctuations in Zr solubility, resulting in a consistent distribution between cassiterite and the aqueous fluid. Zirconium solubility is also sensitive to changes in pH, although this effect is subordinate to the control imparted by the concentration of Si in the fluid (Ayers et al. 2012). Nevertheless, if the system is assumed to remain Si saturated throughout mineralization, then this suggests that changes in the Zr content of cassiterite may record changes in pH during crystallization.

B. Magmatic Systems. Some oscillatory zonation is observable in the X-ray element maps for the White Lode crystal (Figure 12) despite this not being detectable via CL imaging. The zonation appears to be driven by the coupled Fe-Nb-Ta substitution mechanism of equation 2. This may be described in terms of intrinsic variables if the boundary layer model of crystal growth is applied (Allègre et al. 1981; Ortoleva 1990; Shore and Fowler 1996). Under non-equilibrium conditions, a finite region may envelop the growing crystal with a composition that deviates from the bulk melt due to the interplay between the crystal growth rate and the diffusion

rates of solutes towards (or away from) the growth face. In this case, the individual diffusivities of Fe, Nb and Ta through the boundary layer may develop patterns only seen in these elements. Titanium would be less sensitive in this model, as it only requires diffusion of one component through the boundary layer. This could explain the lack of distinct fine scale oscillatory zonation of Ti observed in this sample (Figure 12).

Similarly, an extrinsic explanation for oscillatory zonation requires a variable that strongly affects Fe-Nb-Ta but not Ti within a silicate liquid. Changes to bulk composition, temperature and pressure are unlikely to be defining variables in this case, as these would presumably also act upon Ti. Oxygen fugacity would also have little effect upon Ti, but it could affect the Fe^{2+}/Fe^{3+} ratio. This would impart control on the preferred substitution reaction between equations 1 and 2 and could drive the observed oscillations through variable partition coefficients between the two end member components. Further analytical work to quantitatively measure the Fe^{2+}/Fe^{3+} ratio across these oscillatory zones would provide evidence for a preferred model.

Sector Zonation

The crystals examined in this paper show that sector zonation imparts a marked control on the distribution of Fe, Nb, Ta and W in cassiterite. Three compositionally distinct sectors can be identified, characterized by a) high Fe and low W contents, b) low Fe and high W contents, and c) low Fe and low W contents. In line with models for sector zonation in cassiterite (Dowty 1976, Farmer 1991), it is likely that the low Fe and low W zones form along the {110} face because of the 4.5/6 coordination of the protosites. Farmer (1991) reports W enrichment in the {101} sectors of their samples due to the low 3/6 coordination ratio for this surface. This is in agreement with our observations for the low Fe and high W sectors.

The enrichment in Fe in a different sector to that enriched in W, as seen in cassiterite MB1 (Figure 3a versus Figure 3b), raises two interesting points. Firstly, the observed enrichment of Fe with negligible Nb and Ta contents points to the substitution of Fe via equation 4. The charge balance for this reaction is provided via protonation of a neighboring oxygen. Smyth et al. (1995) show that the positioning of OH^- in rutile is oriented in the (001) plane along the shared edges of the 6-fold coordination polyhedra. Assuming a similar structural relationship applies to cassiterite, the sector zonation behavior of Fe^{3+} may be due to the development of growth faces with favorable geometries for the incorporation of OH^-. The orientation of crystal faces observed in crystal MB1 suggests the {100} sectors provide the most favorable geometry, and this would serve as a distinction to the {101} sectors, which have the same 3/6 protosite coordination ratio but only show W enrichment. Additionally, the {101} sectors may provide a more favorable geometry for the incorporation of W due to its common existence as an oxytungstate anion in geological environments (Wood and Samson 2000). This could explain the lack of W in the {100} sectors if those growth faces have an unsuitable topology.

Secondly, the incorporation mechanism for W in the cassiterite crystals from Mount Bischoff and Saltwater Creek is not supported by equations 6 (a 1:1 W:Fe atomic ratio) or 7 (a 1:2 W:Fe atomic ratio) due to the low Fe contents observed in the high W sectors, which are in fact closer to a 2:1 W:Fe atomic ratio. The existence of some component of equation 5 (W^{4+} substitution) or a previously unreported substitution mechanism such as a coupled $W^{6+} + W^{4+} + Fe^{2+}$ or a $2W^{5+} + Fe^{2+}$ reaction may be more appropriate in these instances. The discrimination of these possible reactions can be achieved via quantitative measurements on the valence state of W.

Additionally, Ti shows no specific sectoral preference, and the concentrations within the cassiterite crystals examined in this study remain consistent along a given growth band across

different sectors (e.g., Figures 3, 4 and 6). The concentrations of Zr and Mn within the samples studied are too low to discriminate any potential effects of sector zonation upon their internal distribution.

Secondary features

There appear to be two distinct CL features that cross-cut primary growth structures, CL-bright lineations and convolute CL patches. The CL-bright lineations (e.g., Figures 2k, 8d and 11c) are seen in all crystals except for MB2, whilst the overprinting convolute CL patches are only observed in BM1 (Figure 8c), BM2 (Figure 8m) and WL1 (Figure 11b, d). The Sn X-ray element maps show that these features relate to recrystallized cassiterite, although some other mineral inclusions may be present (e.g., Figure 9i), consistent with a fluid mediated recrystallisation reaction. These features also display a depletion in Fe, Nb, Ta and W to concentrations near or below the limit of detection, regardless of the initial concentrations of these elements. In contrast, Ti tends to be slightly enriched (e.g., Figure 9a) with respect to the initial concentration, and tends to be in the order of 0.2 at%. The combined effect of lower Fe, Nb, Ta and W contents along with a small amount of Ti results in a characteristic increase in CL brightness when compared to the host crystal.

In crystal SC2, the subvertical lineations (Figure 5g) are parallel to concentric growth zones (highlighted by Figure 7d, e), which we interpret as the result of failure along the cleavage and parting planes of cassiterite. The higher density of fractures on the left side of the twin plane in this crystal may be a result of the different alignments of the cleavage planes on each side of the crystal with respect to the principal stresses during brittle failure. Assuming the subhorizontal fractures (Figure 5h) postdate the subvertical fractures (based on overprinting relationships), then

610 the change in orientation may be due to a change in the orientation of the principal stresses. It is
611 worth noting that only the hyperspectral CL map for this crystal (Figure 5) highlights the two
612 possible generations of fractures (Figure 5g, h) due to subtle differences in their CL intensity and
613 apparent overprinting relationships. These generations are not distinguishable in the X-ray
614 element maps (Figure 7).

615 Cassiterite crystal BM1 displays an overprinting convolute CL rim (Figure 8c) that appears
616 continuous with a brittle fracture (highlighted in Figures 9a, b), suggesting that the fluids
617 responsible for recrystallisation along the fracture are also responsible for the convolute CL rim.
618 In contrast, in cassiterite crystal WL1 the convolute CL regions are cross-cut by the brittle
619 fractures (Figure 11g), suggesting two separate stages of fluid alteration in this case.

620 These mottled or convolute CL regions are likely the result of dissolution-precipitation reactions
621 due to their prevalence near the rims of these crystals. Similarly, these disturbed complex
622 structures have also been observed in CL imagery in zircon, where they have been ascribed a
623 similar model of formation (Corfu et al. 2003). The dominant driver of the dissolution-
624 precipitation reaction in zircon is metamictization in old and/or very U-rich crystals (Geisler et
625 al. 2001, 2002, 2003, 2007). However, metamictization is likely to be negligible in cassiterite, as
626 U contents have only been reported up to 50 ppm (Yuan et al. 2011; Zhang et al. 2017; Deng et
627 al. 2018). Other research on dissolution-precipitation processes have developed models through
628 research on the relative solubilities of various alkali halides (Glynn and Reardon 1990; Putnis
629 and Mezger 2004; Pollok et al. 2011; Ruiz-Agudo et al. 2014). These mechanisms describe
630 replacement processes in binary systems (with or without solid solution) and are aimed at
631 describing pseudomorphism, but they may have some utility towards describing the processes
632 involved in cassiterite alteration.

633 **CL-dark crystals**

634 The complex history recorded in cassiterite crystals BM2 and WL1 were not revealed via
635 standard panchromatic CL imagery (Figures 8 and 11, respectively). The generally low
636 panchromatic CL response from crystal BM2 (Figure 8) is the result of low Ti contents in most
637 of the crystal. Where Ti concentrations would be high enough to return a bright CL response, the
638 sum of Fe, Nb and W contents result in quenched activity for these regions. Combining
639 information from the hyperspectral CL and X-ray element maps indicates that crystal BM2 has
640 experienced multiple growth stages that include early and late dissolution-reprecipitation
641 processes. These generated the patchy embayed cores (Figure 8g-j), the CL-bright overprinting
642 rim (Figure 8m), and a network of recrystallized fractures (Figure 8n).

643 Crystal WL1 shows no primary growth structures in either panchromatic or hyperspectral CL
644 images, however the hyperspectral CL image allows for the delineation of CL-bright healed
645 fractures and convolute CL dissolution-precipitation regions. The X-ray element maps (Figure
646 12) show a primary oscillatory growth stage rich in Fe, Nb and Ta (region B). Combining
647 observations from both the hyperspectral CL and X-ray element maps allows for the formulation
648 of a paragenetic interpretation (Figure 13). The primary growth stage (blue regions, Figure 13a)
649 is characterized by low Sn contents in the X-ray element maps, and the regions of convolute CL
650 are illustrated in purple (Figure 13b). The numerous inclusions throughout the sample tend to be
651 associated with the convolute CL regions and the CL-bright fractures (Figure 13), suggesting that
652 these are likely related to dissolution-reprecipitation processes and not the products of exsolution
653 during cooling.

Interestingly, while the convolute CL regions correlate with regions that approach pure SnO_2, there also remain regions of high Sn purity that have no corresponding CL signature, illustrated in orange (Figure 13c).

One particular area of this CL non-responsive high Sn region (Figure 13d) is apparently euhedral, and in optical alignment with the rest of the crystal. This raises two interesting possibilities. Firstly, this region may be interpreted as a distinct paragenetic stage of alteration, bound by crystallographic planes by an unknown physical mechanism. If this is the case, then not all secondary alteration processes may result in a CL signature, and to our knowledge this may be the first recorded example of CL-dark alteration in cassiterite. Secondly, this region may be interpreted as a paragenetically early euhedral crystal, enveloped within the larger oscillatory zoned host crystal. In this case, the optical continuity of the crystal may be explained via synneusis, a process where individual crystals suspended in a magma drift together and join in crystallographic alignment (Vance 1969; Schwindinger and Anderson 1989). This also would be the first evidence for synneusis in cassiterite to our knowledge. The oscillatory zonation, however, does not envelope the region and is instead truncated by it, which leads us to favor the first possibility. Regardless of which model is correct, the ambiguity of this region is only apparent after consideration of both the hyperspectral CL and X-ray element maps, the sole use of either would not allow for the clear distinction we present here.

IMPLICATIONS

Cathodoluminescence characterization of cassiterite

The Fe, Nb, Ta and W depletion effects of the brittle fractures and convolute CL overprinting regions usually result in a relative increase in CL brightness, allowing these secondary features

676 to be identified via CL imaging, but this may not always be the case due to the initial high Fe,
677 Nb, Ta and W contents in some cassiterite samples. In addition, certain localities may have
678 internal microstructures that are either difficult to identify (e.g., BM2) or invisible (e.g., WL1)
679 utilizing only CL techniques. In these cases, identification of primary (and some secondary)
680 growth microstructures requires quantitative X-ray element mapping. However, the differences
681 in chemistry between distinct generations of secondary features are usually too subtle to be
682 distinguished by quantitative EPMA X-ray mapping and are best resolved through hyperspectral
683 CL mapping. Thus, a combination of hyperspectral CL and quantitative EPMA X-ray mapping is
684 an essential prerequisite for more complete characterization of samples prior to in situ analysis.

685 **Secondary alteration processes in cassiterite**

686 The cross-cutting structures identified in the present study remobilize Ti, at least locally, and
687 appear to decrease the original contents of other elements substituted into the cassiterite lattice
688 during growth. Using only CL techniques to detect potential secondary alteration (and hence
689 isotopic disturbance) thus relies on the mobility of Ti in the late stage fluids, and in some
690 instances, it appears that Ti has in fact been enriched (e.g., Figures 7f, 9a, 10k). This is probably
691 due to the requirement that any dissolution-precipitation processes in cassiterite also require Sn
692 mobility, and a fluid capable of the local mobilization of Sn is probably capable of locally
693 mobilizing Ti. These overprinting structures are likely to reflect late stage mineralization
694 processes, and thus would nominally be close in age to the main stage mineralization event.
695 These domains may, however, show significant variability in oxygen isotopes or in other
696 chemical indices sensitive to different fluid sources. While U-Pb dating of these regions may
697 help resolve the timing of events in complex mineralized systems with a protracted history, if the

main research goal is to establish the primary tin mineralization age then these areas have a high potential for disturbance to the U-Pb system and are best avoided.

Interpretation of sample population variability via grain mounts

Common practice for zircon geochronology involves crushing and milling of bulk rock samples to extract the zircon crystals, and a similar technique has been applied in some recent cassiterite U-Pb studies (e.g., Carr et al. 2017; Neymark et al. 2018; Cheng et al. 2019; Zhang et al. 2019). As cassiterite crystals tend to be large (>1mm in most mineralized systems) this process results in numerous small fragments of cassiterite, which are then hand-picked and mounted in an epoxy disk. If these fragments are characterized by their cathodoluminescent properties or their minor element contents alone, multiple populations might be suspected or inferred due to the contrasting responses of different sector zones within the original crystals. This is also a risk for cassiterite fragments generated naturally via alluvial transport. For instance, the presence of high and low W cassiterite fragments might be interpreted as the existence of two separate mineralized deposits in the sediment provenance. This potentially erroneous interpretation might be avoided through the selection of the largest grains possible to capture these zones in the same crystal.

Examination of grains within a thin section can provide not only intact crystals, but also paragenetic relationships in the case of multiple cassiterite generations and is thus the most ideal approach.

Acquisition of in situ trace element data

Quantitative trace element analyses via in situ methods (such as LA-ICP-MS or SIMS) requires an internal elemental standard for calibration of the other analyte elements. Current best practice

720 is to use the concentration of a minor component of the mineral as measured by EPMA, e.g., Hf
721 in zircon. For cassiterite, Fe or Ti are the best candidates as they are present in all samples
722 analyzed for this study and are commonly reported in the literature; however, care must be taken
723 to account for the fine scale oscillatory zonation that can vary by an order of magnitude across
724 the interval of the analysis spot size. Zirconium might be considered as an alternative due to its
725 low internal variability, but its concentration is frequently within uncertainty of the 99%
726 confidence limit of detection. This may result in an unnecessary propagation of uncertainties in
727 the final calculation of absolute concentration, which would negate any benefit in using Zr over
728 Ti or Fe.

729 **A detailed record of mineral system dynamics**

730 If the oscillatory character of Fe, Nb, Ta and W in hydrothermal-metasomatic cassiterite crystals
731 are driven by extrinsic factors, and models describing these variables can be established, then the
732 fluid evolution of the ore forming environment may be deconvolved during the stages of
733 cassiterite precipitation. However, the use of these elemental contents may be limited in crystals
734 that did not develop the required growth faces for their incorporation. The fact that Ti does not
735 display sensitivity to sector zonation means that its strong oscillatory character may be useful as
736 an internal ‘stratigraphic’ signature for cross correlation between multiple crystals of cassiterite
737 in protracted paragenetic stages.

738 If the oscillatory character of one or more of these elements is instead driven by intrinsic factors,
739 then the recognition of this process is crucial for the processing of trace element or stable
740 isotopic data, which may have a fundamentally different interpretation in systems far from
741 equilibrium.

Detailed imaging of cassiterite by multiple techniques elucidate that this mineral may contain evidence for a surprisingly complex growth and secondary alteration history. This may vary according to different mineralization environments and provide new insights into the mineralizing environment for Sn and the behavior of associated rare metals.

ACKNOWLEDGMENTS

The authors would like to thank Steffen Hagemann and Marco Fiorentini for valuable comments and discussion, as well as Richard J. Moscati and an anonymous reviewer for their insightful feedback, which significantly improved this manuscript. We also thank Nilson F. Botelho and Mathew Latham for providing samples used in this research. The authors acknowledge the facilities, and the scientific and technical assistance of the Australian Microscopy & Microanalysis Research Facility at the Centre for Microscopy, Characterisation & Analysis, The University of Western Australia, a facility funded by the University, State and Commonwealth Governments. Jason M. Bennett was supported by an Australian Government Research Training Program (RTP) Scholarship, and acknowledges support from the Australian Research Council through the ARC Centre of Excellence for Core to Crust Fluid Systems (CE110001017). This is contribution 1372 from the ARC Centre of Excellence for Core to Crust Fluid Systems (http://www.ccfs.mq.edu.au).

REFERENCES

Allègre, C.J., Provost, A., and Jaupart, C. (1981) Oscillatory zoning: A pathological case of crystal growth. Nature, 294, 223–228.

Ayers, J.C., Zhang, L., Luo, Y., and Peters, T.J. (2012) Zircon solubility in alkaline aqueous fluids at upper crustal conditions. Geochimica et Cosmochimica Acta, 96, 18–28.

764 Beurlen, H., Thomas, R., da Silva, M.R.R., and Silva, D. (2007) Manganocolumbite and cassiterite exsolution
765 lamellae in ilmenite from the Pitombeiras pegmatite (Acari - Rio Grande Do Norte) in the Borborema
766 pegmatitic province, NE-Brazil. Estudos Geológicos, 16, 3–15.

767 Blevin, P.L., and Norman, M.D. (2010) [Poster] Cassiterite: The zircon of mineral systems - A scoping study,
768 Australian Earth Science Convention 2010, AESC2010. Poster GS2010/0483.

769 Bolzan, A.A., Fong, C., Kennedy, B.J., and Howard, C.J. (1997) Structural Studies of Rutile-Type Metal Dioxides.
770 Acta Crystallographica Section B Structural Science, 53, 373–380.

771 Botelho, N.F., and Moura, M.A. (1998) Granite-ore deposit relationships in Central Brazil. Journal of South
772 American Earth Sciences, 11, 427–438.

773 Brantley, S.L., Evans, B., Hickman, S.H., and Crerar, D.A. (1990) Healing of microcracks in quartz: Implications
774 for fluid flow. Geology, 18, 136.

775 Carr, P.A., Norman, M.D., and Bennett, V.C. (2017) Assessment of crystallographic orientation effects on
776 secondary ion mass spectrometry (SIMS) analysis of cassiterite. Chemical Geology, 467, 122–133.

777 Chakhmouradian, A.R., Smith, M.P., and Kynicky, J. (2015) From “strategic” tungsten to “green” neodymium: A
778 century of critical metals at a glance. Ore Geology Reviews, 64, 455–458.

779 Cheng, Y., Mao, J., Chang, Z., and Pirajno, F. (2013) The origin of the world class tin-polymetallic deposits in the
780 Gejiu district, SW China: Constraints from metal zoning characteristics and ^{40}Ar-^{39}Ar geochronology. Ore
781 Geology Reviews, 53, 50–62.

782 Cheng, Y., Spandler, C., Kemp, A., Mao, J., Rusk, B., Hu, Y., and Blake, K. (2019) Controls on cassiterite (SnO_2)
783 crystallization: Evidence from cathodoluminescence, trace-element chemistry, and geochronology at the Gejiu
784 Tin District. American Mineralogist, 104, 118–129.

785 Cherniak, D.., and Watson, E.. (2001) Pb diffusion in zircon. Chemical Geology, 172, 5–24.

786 Cherniak, D.J., Manchester, J., and Watson, E.B. (2007) Zr and Hf diffusion in rutile. Earth and Planetary Science
787 Letters, 261, 267–279.

788 Clayton, R.E., and Rojkovic, I. (1999) Lead isotopes in cassiterite:- some preliminary experiments and their
789 geoarchaeological significance. Geoscience in south west England, 9, 340–346.

790 Corfu, F., Hanchar, J.M., Hoskin, P.W.O., and Kinny, P.D. (2003) Atlas of zircon textures. Reviews in Mineralogy
791 and Geochemistry, 53, 469–500.

792 Deng, X.-H., Chen, Y.-J., Bagas, L., Zhou, H.-Y., Zheng, Z., Yue, S.-W., Chen, H.-J., Li, H.-M., Tu, J.-R., and Cui,
793 Y.-R. (2018) Cassiterite U-Pb geochronology of the Kekekaerde W-Sn deposit in the Baiganhu ore field, East
794 Kunlun Orogen, NW China: Timing and tectonic setting of mineralization. Ore Geology Reviews, 100, 534–
795 544.

796 Donovan, J.J. (2018) CalcImage v12.3.7. Probe Software, Inc.

797 Dowty, E. (1976) Crystal structure and crystal growth: II. Sector zoning in minerals. American Mineralogist, 61,
798 460–469.

799 Dusausoy, Y., Ruck, R., and Gaite, J.M. (1988) Study of the symmetry of Fe^{3+} sites in SnO_2 by electron
800 paramagnetic resonance. Physics and Chemistry of Minerals, 15, 300–303.

801 Farmer, C.B. (1991) Cathodoluminescence and Growth of Cassiterite in the Composite Lodes at South Crofty Mine,
802 Cornwall, England. Mineralogical Magazine, 55, 447–458.

803 Ferry, J.M., and Watson, E.B. (2007) New thermodynamic models and revised calibrations for the Ti-in-zircon and
804 Zr-in-rutile thermometers. Contributions to Mineralogy and Petrology, 154, 429–437.

805 Fromknecht, R., Khubeis, I., and Meyer, O. (1996) La-, Sn- and Hf-implanted in TiO_2 single crystals: lattice
806 disorder and lattice site location. Nuclear Instruments and Methods in Physics Research B, 116, 109–112.

807 Frondel, C., Newhouse, W., and Jarrell, R.F. (1942) Spatial distribution of minor elements in single-crystals.
808 American Mineralogist, 27, 726–745.

809 Galliski, M.Á., Márquez-Zavalía, M.F., Černý, P., and Lira, R. (2016) Complex Nb-Ta-Ti-Sn Oxide Mineral
810 Intergrowths In The La Calandria Pegmatite, Cañada Del Puerto, Córdoba, Argentina. The Canadian
811 Mineralogist, 54, 899–916.

812 Geisler, T., Ulonska, M., Schleicher, H., Pidgeon, R.T., and van Bronswijk, W. (2001) Leaching and differential
813 recrystallization of metamict zircon under experimental hydrothermal conditions. Contributions to Mineralogy
814 and Petrology, 141, 53–65.

815 Geisler, T., Pidgeon, R.T., van Bronswijk, W., and Kurtz, R. (2002) Transport of uranium, thorium, and lead in
816 metamict zircon under low-temperature hydrothermal conditions. Chemical Geology, 191, 141–154.

817 Geisler, T., Pidgeon, R.T., Kurtz, R., van Bronswijk, W., and Schleicher, H. (2003) Experimental hydrothermal
818 alteration of partially metamict zircon. American Mineralogist, 88, 1496–1513.

819 Geisler, T., Schaltegger, U., and Tomaschek, F. (2007) Re-equilibration of Zircon in Aqueous Fluids and Melts.
820 Elements, 3, 43–50.

821 Glynn, P.D., and Reardon, E.J. (1990) Solid-solution aqueous-solution equilibria; thermodynamic theory and
822 representation. American Journal of Science, 290, 164–201.

823 Grundmann, G., and Morteani, G. (1998) Alexandrite, emerald, ruby, sapphire and topaz in a biotite-phlogopite fels
824 from Poona, Cue District, Western Australia. Australian Gemmologist, 20, 159--167.

825 Gulson, B.L., and Jones, M.T. (1992) Cassiterite: Potential for direct dating of mineral deposits and a precise age for
826 the Bushveld Complex granites. Geology, 20, 355.

827 Guo, J., Zhang, R., Li, C., Sun, W., Hu, Y., Kang, D., and Wu, J. (2018) Genesis of the Gaosong Sn–Cu deposit,
828 Gejiu district, SW China: Constraints from in situ LA-ICP-MS cassiterite U–Pb dating and trace element
829 fingerprinting. Ore Geology Reviews, 92, 627–642.

830 Halden, N., and Hawthorne, F. (1993) The fractal geometry of oscillatory zoning in crystals: Application to zircon.
831 American Mineralogist, 78, 1113–1116.

832 Hall, M.R., and Ribbe, P.H. (1971) An Electron Microprobe Study of Luminescence Centers in Cassiterite. The
833 American Mineralogist, 56, 31–45.

834 Halley, S.W., and Walshe, J.L. (1995) A reexamination of the Mount Bischoff cassiterite sulfide skarn, western
835 Tasmania. Economic Geology, 90, 1676–1693.

836 Holten, T., Jamtveit, B., Meakin, P., Cortini, M., Blundy, J., and Austrheim, H. (1997) Statistical characteristics and
837 origin of oscillatory zoning in crystals. American Mineralogist, 82, 596–606.

838 Holten, T., Jamtveit, B., and Meakin, P. (2000) Noise and oscillatory zoning of minerals. Geochimica et
839 Cosmochimica Acta, 64, 1893–1904.

840 Izoret, L., Marnier, G., and Dusausoy, Y. (1985) Caracterisation cristallochimique de la cassiterite des gisements
841 d'etain et de tungstene de Galice, Espagne. The Canadian Mineralogist, 23, 221–231.

842 Jambor, J.L., Pertsev, N.N., and Roberts, A.C. (1995) New Mineral Names - Varlamoffite. American Mineralogist,
843 80, 845–850.

844 Jamtveit, B. (1991) Oscillatory zonation patterns in hydrothermal grossular-andradite garnet: nonlinear dynamics in
845 regions of immiscibility. American Mineralogist, 76, 1319–1327.

846 Jamtveit, B., and Hervig, R.L. (1994) Constraints on Transport and Kinetics in Hydrothermal Systems from Zoned
847 Garnet Crystals. Science, 263, 505–508.

848 Jamtveit, B., Agnarsdottir, K.V., and Wood, B.J. (1995) On the origin of zoned grossular-andradite garnets in
849 hydrothermal systems. European Journal of Mineralogy, 7, 1399–1410.

850 Keid, H.G.W. (1951) Memorandum - Investigation Lease No. 31M/50 Coles Bay, 70–73 p. MRT Document
851 UR1951_070_73. Mineral Resources Tasmania, Hobart.

852 Kelly, W.C., and Rye, R.O. (1979) Geologic, fluid inclusion, and stable isotope studies of the tin-tungsten deposits
853 of Panasqueira, Portugal. Economic Geology, 74, 1721–1822.

854 Korotcenkov, G., Nazarov, M., Zamoryanskaya, M. V., Ivanov, M., Cirera, A., and Shimanoe, K. (2006)
855 Cathodoluminescence study of SnO_2 powders aimed for gas sensor applications. Materials Science and
856 Engineering B: Solid-State Materials for Advanced Technology, 130, 200–205.

857 L'Heureux, I., and Jamtveit, B. (2002) A model of oscillatory zoning in solid solutions grown from aqueous
858 solutions: Applications to the (Ba,Sr) SO4system. Geochimica et Cosmochimica Acta, 66, 417–429.

859 Lenharo, S.L.., Moura, M.A., and Botelho, N.F. (2002) Petrogenetic and mineralization processes in Paleo- to
860 Mesoproterozoic rapakivi granites: examples from Pitinga and Goiás, Brazil. Precambrian Research, 119,
861 277–299.

862 Li, C., Zhang, R., Ding, X., Ling, M., Fan, W., and Sun, W. (2016) Dating cassiterite using laser ablation ICP-MS.
863 Ore Geology Reviews, 72, 313–322.

864 Liu, Y., Li, Z., Li, H., Guo, L., Xu, W., Ye, L., Li, C., and Pi, D. (2007) U-Pb geochronology of cassiterite and
865 zircon from the Dulong Sn-Zn deposit: Evidence for Cretaceous large-scale granitic magmatism and
866 mineralization events in southeastern Yunnan province, China. Acta Petrologica Sinica, 23, 967–976.

867 Lopez, L., Jovic, S.M., Guido, D.M., Permuy Vidal, C., Páez, G.N., and Ruiz, R. (2015) Geochemical distribution
868 and supergene behavior of indium at the Pingüino epithermal polymetallic vein system, Patagonia, Argentina.
869 Ore Geology Reviews, 64, 747–755.

870 Losos, Z., and Beran, A. (2004) OH defects in cassiterite. Mineralogy and Petrology, 81, 219–234.

871 Maestre, D., Ramírez-Castellanos, J., Hidalgo, P., Cremades, A., González-Calbet, J.M., and Piqueras, J. (2007)
872 Study of the defects in sintered SnO_2 by high-resolution transmission electron microscopy and
873 cathodoluminescence. European Journal of Inorganic Chemistry, 1544–1548.

874 Maldener, J., Rauch, F., Gavranic, M., and Beran, A. (2001) OH absorption coefficients of rutile and cassiterite
875 deduced from nuclear reaction analysis and FTIR spectroscopy. Mineralogy and Petrology, 71, 21–29.

876 Marshall, D., Downes, P., Ellis, S., Greene, R., Loughrey, L., and Jones, P. (2016) Pressure–Temperature–Fluid
877 Constraints for the Poona Emerald Deposits, Western Australia: Fluid Inclusion and Stable Isotope Studies.
878 Minerals, 6, 130.

879 Masau, M., Cerny, P., and Chapman, R. (2000) Exsolution of Zirconian-Hafnian Wodginite From Manganoan-
880 Tantalian Cassiterite, Annie Claim #3 Granitic Pegmatite, Southeastern Manitoba, Canada. The Canadian
881 Mineralogist, 38, 685–694.

882 McNaughton, N.J., Pollard, P.J., Gulson, B.L., and Jones, M.T. (1993) Cassiterite: Potential for direct dating of

883 mineral deposits and a precise age for the Bushveld Complex granites: Comment and Reply. Geology, 21,
884 285.

885 Mezger, K., Hanson, G.N., and Bohlen, S.R. (1989) High-precision UPb ages of metamorphic rutile: application to
886 the cooling history of high-grade terranes. Earth and Planetary Science Letters, 96, 106–118.

887 Möller, P., Dulski, P., Szacki, W., Malow, G., and Riedel, E. (1988) Substitution of tin in cassiterite by tantalum,
888 niobium, tungsten, iron and manganese. Geochimica et Cosmochimica Acta, 52, 1497–1503.

889 Moscati, R.J., and Neymark, L.A. (2019) U–Pb geochronology of tin deposits associated with the Cornubian
890 Batholith of southwest England: Direct dating of cassiterite by in situ LA-ICPMS. Mineralium Deposita.

891 Nakamura, Y. (1973) Origin of Sector-Zoning of lgneous Clinopyroxenes. American Mineralogist, 58, 986–990.

892 Nasdala, L. (2003) Spectroscopic methods applied to zircon. Reviews in Mineralogy and Geochemistry, 53, 427–
893 467.

894 Neiva, A.M.R. (1996) Geochemistry of cassiterite and its inclusions and exsolution products from tin and tungsten
895 deposits in Portugal. Canadian Mineralogist, 34, 745–768.

896 Neiva, A.M.R. (2008) Geochemistry of cassiterite and wolframite from tin and tungsten quartz veins in Portugal.
897 Ore Geology Reviews, 33, 221–238.

898 Neymark, L.A., Holm-Denoma, C.S., and Moscati, R.J. (2018) In situ LA-ICPMS U–Pb dating of cassiterite without
899 a known-age matrix-matched reference material: Examples from worldwide tin deposits spanning the
900 Proterozoic to the Tertiary. Chemical Geology, 483, 410–425.

901 Ortoleva, P.J. (1990) Role of attachment kinetic feedback in the oscillatory zoning of crystals grown from melts.
902 Earth-Science Reviews, 29, 3–8.

903 Partington, G.A., McNaughton, N.J., and Williams, I.S. (1995) A review of the geology, mineralization, and
904 geochronology of the Greenbushes Pegmatite, Western Australia. Economic Geology, 90, 616–635.

905 Pollok, K., Putnis, C. V., and Putnis, A. (2011) Mineral replacement reactions in solid solution-aqueous solution

systems: Volume changes, reactions paths and end-points using the example of model salt systems. American Journal of Science, 311, 211–236.

Putnis, A., Fernandez-Diaz, L., and Prieto, M. (1992) Experimentally produced oscillatory zoning in the (Ba,Sr)SO_4 solid solution. Nature, 358, 743–745.

Putnis, C. V., and Mezger, K. (2004) A mechanism of mineral replacement: isotope tracing in the model system KCl-KBr-H2O. Geochimica et Cosmochimica Acta, 68, 2839–2848.

Rapp, J.F., Klemme, S., Butler, I.B., and Harley, S.L. (2010) Extremely high solubility of rutile in chloride and fluoride-bearing metamorphic fluids: An experimental investigation. Geology, 38, 323–326.

Reeder, R.J., Fagioli, R.O., and Meyers, W.J. (1990) Oscillatory zoning of Mn in solution-grown calcite crystals. Earth Science Reviews, 29, 39–46.

Ruck, R., Dusausoy, Y., Nguyen Trung, C., Gaite, J.-M., and Murciego, A. (1989) Powder EPR study of natural cassiterites and synthetic SnO_2 doped with Fe, Ti, Na and Nb. European Journal of Mineralogy, 1, 343–352.

Ruiz-Agudo, E., Putnis, C. V., and Putnis, A. (2014) Coupled dissolution and precipitation at mineral-fluid interfaces. Chemical Geology, 383, 132–146.

Salviati, G., Lazzarini, L., Zha, M.Z., Grillo, V., and Carlino, E. (2005) Cathodoluminescence spectroscopy of single SnO_2 nanowires and nanobelts. physica status solidi (a), 202, 2963–2970.

Schwindinger, K.R., and Anderson, A.T. (1989) Synneusis of Kilauea Iki olivines. Contributions to Mineralogy and Petrology, 103, 187–198.

Sharko, E.D. (1971) Nature and properties of varlamoffite (oxidation products of stannite). International Geology Review, 13, 603–614.

Shore, M., and Fowler, A.D. (1996) Oscillatory zoning in minerals: A common phenomenon. Canadian Mineralogist, 34, 1111–1126.

Smith, D.L., and Evans, B. (1984) Diffusional crack healing in quartz. Journal of Geophysical Research: Solid

929 Earth, 89, 4125–4135.

930 Smyth, J.R., Swope, R.J., and Pawley, A.R. (1995) H in rutile-type compounds: II. Crystal chemistry of Al
931 substitution in H-bearing stishovite. American Mineralogist, 80, 454–456.

932 Swope, R.J., Smyth, J.R., and Larson, A.C. (1995) H in rutile-type compounds: I. Single-crystal neutron and X-ray
933 diffraction study of H in rutile. American Mineralogist, 80, 448–453.

934 Tallarico, F.H.B., McNaughton, N.J., Groves, D.I., Fletcher, I.R., Figueiredo, B.R., Carvalho, J.B., Rego, J.L., and
935 Nunes, A.R. (2004) Geological and SHRIMP II U-Pb constraints on the age and origin of the Breves Cu-Au-
936 (W-Bi-Sn) deposit, Carajás, Brazil. Mineralium Deposita, 39, 68–86.

937 Thompson, J.F.H., Sillitoe, R.H., Baker, T., Lang, J.R., and Mortensen, J.K. (1999) Intrusion-related gold deposits
938 associated with tungsten-tin provinces. Mineralium Deposita, 34, 323–334.

939 Tomkins, H.S., Powell, R., and Ellis, D.J. (2007) The pressure dependence of the zirconium-in-rutile thermometer.
940 Journal of Metamorphic Geology, 25, 703–713.

941 Twelvetrees, W.H. (1901) Report of the coalfield of Llandaff, the Denison and Douglas Rivers, on deposits of tin
942 ore on Schouten Main, and on outcrops of quartz near Buckland, 65 p. Launceston.

943 Vance, J.A. (1962) Zoning in igneous plagioclase; normal and oscillatory zoning. American Journal of Science, 260,
944 746–760.

945 Vance, J.A. (1969) On synneusis. Contributions to Mineralogy and Petrology, 24, 7–29.

946 Wille, G., Lerouge, C., and Schmidt, U. (2018) A multimodal microcharacterisation of trace-element zonation and
947 crystallographic orientation in natural cassiterite by combining cathodoluminescence, EBSD, EPMA and
948 contribution of confocal Raman-in-SEM imaging. Journal of Microscopy, 270, 309–317.

949 Wood, S.A., and Samson, I.M. (2000) The Hydrothermal Geochemistry of Tungsten in Granitoid Environments: I.
950 Relative Solubilities of Ferberite and Scheelite as a Function of T, P, pH, and mNaCl. Economic Geology, 95,
951 143–182.

952 Yan, Q., Qiu, Z., Wang, H., Wang, M., Wei, X., Li, P., Zhang, R., Li, C., and Liu, J. (2016) Age of the Dahongliutan
953 rare metal pegmatite deposit, West Kunlun, Xinjiang (NW China): Constraints from LA–ICP–MS U–Pb
954 dating of columbite-(Fe) and cassiterite. Ore Geology Reviews.

955 Yardley, B.W.D., Rochelle, C.A., Barnicoat, A.C., and Lloyd, G.E. (1991) Oscillatory Zoning in Metamorphic
956 Minerals - an Indicator of Infiltration Metasomatism. Mineralogical Magazine, 55, 357–365.

957 Yuan, S., Peng, J., Hao, S., Li, H., Geng, J., and Zhang, D. (2011) In situ LA-MC-ICP-MS and ID-TIMS U–Pb
958 geochronology of cassiterite in the giant Furong tin deposit, Hunan Province, South China: New constraints on
959 the timing of tin–polymetallic mineralization. Ore Geology Reviews, 43, 235–242.

960 Zack, T., Moraes, R., and Kronz, A. (2004) Temperature dependence of Zr in rutile: Empirical calibration of a rutile
961 thermometer. Contributions to Mineralogy and Petrology, 148, 471–488.

962 Zhang, D., Peng, J., Coulson, I.M., Hou, L., and Li, S. (2014) Cassiterite U–Pb and muscovite ^{40}Ar–^{39}Ar age
963 constraints on the timing of mineralization in the Xuebaoding Sn–W–Be deposit, western China. Ore Geology
964 Reviews, 62, 315–322.

965 Zhang, R., Lu, J., Wang, R., Lu, X., Guo, J., Li, F., Lehmann, B., Yao, Y., and Guo, W. (2013) Contrasting W and
966 Sn mineralization events and related granitoids in Wangxianling-Hehuaping area, Nanling Range, South
967 China. In Mineral Deposit Research for a High-Tech World. 12th SGA Biennial Meeting pp. 1343–1346.

968 Zhang, R., Lehmann, B., Seltmann, R., Sun, W., and Li, C. (2017) Cassiterite U-Pb geochronology constrains
969 magmatic-hydrothermal evolution in complex evolved granite systems: The classic Erzgebirge tin province
970 (Saxony and Bohemia). Geology, 45, 1095–1098.

971 Zhang, S., Zhang, R., Lu, J., Ma, D., Ding, T., Gao, S., and Zhang, Q. (2019) Neoproterozoic tin mineralization in
972 South China: geology and cassiterite U–Pb age of the Baotan tin deposit in northern Guangxi. Mineralium
973 Deposita.

974

975

This is a preprint, the final version is subject to change, of the American Mineralogist (MSA)
Cite as Authors (Year) Title. American Mineralogist, in press.
DOI: https://doi.org/10.2138/am-2020-6964

976

977 **Table 1:** Cathodoluminescent microstructural characteristics of cassiterite examined in this study

Texture	Localities	Samples
Concentric Zonation	Mount Bischoff, Tasmania, Australia	MB1, MB2
	Saltwater Creek, Tasmania, Australia	SC1, SC2
	Buriti Mine, Goiás, Brazil	BM1
Sector Zonation	Mount Bischoff, Tasmania, Australia	MB1, MB2
	Saltwater Creek, Tasmania, Australia	SC1, SC2
	Buriti Mine, Goiás, Brazil	BM2
Secondary Features	Saltwater Creek, Tasmania, Australia	SC2
	Buriti Mine, Goiás, Brazil	BM1
CL-Dark Crystals	Buriti Mine, Goiás, Brazil	BM2
	White Lode, Western Australia, Australia	WL1

978

979 **Table 2:** Summary of localities for the cassiterite crystals examined in this study

Name	State, Country	Latitude, Longitude	Mineralization Style	References
Mount Bischoff	Tasmania, Australia	-41.43°, 145.52°	cassiterite-sulfide skarn	Halley and Walshe (1995)
Saltwater Creek	Tasmania, Australia	-42.11°, 148.27°	alluvial (greisen or quartz-vein)	Twelvetrees (1901) Keid (1951)
Buriti	Goiás, Brazil	-13.53°, -48.53°	hydrothermal albitite (greisen)	Botelho and Moura (1998) Lenharo et al. (2002)
White Lode	Western Australia, Australia	-27.13°, 117.46°	Sn-granite (magmatic)	Grundmann and Morteani (1998) Marshall et al. (2016)

980

981

982

983 **Table 3:** Cassiterite analysis routine and standards for quantitative X-ray element maps

Element/Line	Crystal	Count Time (s)	Standard
Sn lα	PETJ	40	Cassiterite
Ti kα	PETJ	50	Rutile
Fe kα	LiF	40	Magnetite
Mn kα	LiF	40	Mn
W lα	LiF	40	Scheelite
Ta lα	LiF	50	Manganotantalite
Nb lα	PETH	40	$CaNb_2O_6$
Zr lα	PETH	60	Zr
Si kα	TAP	20	Jadeite
Al kα	TAP	40	Corundum

984

985

Figure 1. Plane polarized light photomicrographs of cassiterite MB1 from Mount Bischoff, comparing transmitted light (**left**) with reflected light (**right**). In transmitted light, concentric growth domains are identifiable by non-pleochroic bands of variable intensity with an inner light-brown core (**a**), a colorless central domain (**b**), a dark-brown outer domain (**c**), and a colorless rim (**d**). The darkest regions (**e, f**) do not exhibit pleochroism. Twin planes can be observed in reflected light, denoted by the white dashed lines. Sellaite (**Sel**) and quartz (**Qz**) form euhedral crystals along with the cassiterite (**Cst**).

Figure 2. Cathodoluminescence imaging of cassiterite crystals MB1 and MB2 from Mount Bischoff, comparing panchromatic (**left**) with hyperspectral imaging (**right**). The hyperspectral maps are false colored, with blue assigned to 200-500 nm, green to 500-600 nm and red to 600-900 nm. See text for discussion of oscillatory zonation features labelled (**a**), (**b**), (**c**), and (**d**), individual CL-dark bands such as (**e**) and (**f**), the dark blue sector zones (**g**), (**h**) and (**i**), the red sector zone (**j**), and CL-bright cross-cutting features such as (**k**). Sellaite (**Sel**) appears as the green-yellow-orange euhedral crystals in the hyperspectral CL map.

Figure 3. X-ray element maps for cassiterite crystal MB1 from Mount Bischoff. Primary growth structures include a distinct Fe-rich concentric growth band (**a**), sector zones that are both W-rich (**b**), (**c**) and Fe-poor (**d**), (**e**), a concentric growth zone with oscillatory zonation in Ti (**f**) and Fe below the detection limit (**g**), and a concentric growth zone with high Ti (**h**) and oscillatory zonation in Fe (**i**). A secondary cross-cutting structure is visible in the Fe map (**j**).

Figure 4. X-ray element maps for cassiterite crystal MB2 from Mount Bischoff. See text for discussion on the concentric growth zone which displays oscillatory Ti (**a**) with Fe

concentrations below the detection limit (**b**), the high Ti growth band (**c**) with Fe below detection (**d**), the high W sector zone (**e**) with moderate to low Fe contents (**f**), the low W concentric growth zone (**g**) with oscillatory zonation in Ti (**h**), and the distinct sector zone with low Fe (**i**) and W concentrations below the detection limit (**j**).

Figure 5. Cathodoluminescence imaging of cassiterite crystals from Saltwater Creek, comparing panchromatic (**left**) with hyperspectral imaging (**right**). The hyperspectral maps are false colored, with blue assigned to 200-500 nm, green to 500-600 nm and red to 600-900 nm. Cassiterite crystal SC1 shows distinct CL-bright (**a**) and CL-dark (**b**) sectors, with oscillatory zoning (**c**) visible in the CL-bright sector. Similar sector zones are visible in cassiterite crystal SC2, with oscillatory zoned CL-bright (**d**), and CL-dark (**e**) sectors. Secondary CL-bright cross-cutting features (**f**) can be split into two generations with different orientations: a subvertical generation (**g**), itself cross-cut by a subhorizontal generation with a brighter CL response (**h**). The red arrows highlight the orientation of each generation. Most of the cross-cutting features are restricted to the left of a twin plane denoted by a dashed line (**i**), although some exist to the right of this plane (**j**). Laser ablation pits (23 μm in diameter) are visible in the hyperspectral maps (**k**), (**l**), along with a darkened CL response due to lattice damage from the electron beam during X-ray element mapping (**m**), (**n**). The white corners denote the X-ray element map areas.

Figure 6. X-ray element maps for cassiterite crystal SC1 from Saltwater Creek. Distinct sector zonation is observed in W, with a sector below the detection limit (**a**) and an oscillatory zoned sector (**b**). A particularly high concentration of Ti (**c**) occurs in a concentric growth zone along with low-moderate Nb contents (**d**). Niobium is generally higher in the W-rich sector zone and displays weak oscillatory character (**e**). Fe is lower in the W-rich sector zone (**f**), and higher in the W-poor sector zone (**g**).

Figure 7. X-ray element maps for cassiterite crystal SC2 from Saltwater Creek. Like SC1 (Figure 6), distinct sector zonation is also observed in this crystal, with Fe-rich (**a**) and W-rich (**b**) sectors. The oscillatory behavior of Nb is observed clearly in this sample (**c**), whereas Ti only shows concentric growth zones (**d**). Weak growth zones are also observed in Fe (**e**). A secondary cross-cutting feature shows Ti contents of around 0.15 at% (**f**), with Fe (**g**), Nb (**h**) and W (**i**) below the limit of detection.

Figure 8. Cathodoluminescence imaging of cassiterite crystals from the Buriti mine, comparing panchromatic (left) with hyperspectral imaging (right). The hyperspectral maps have been colored with blue assigned to 200-500 nm, green to 500-600 nm and red to 600-900 nm. In cassiterite crystal BM1, an oscillatory zoned CL-bright sector (**a**) and a CL-dark sector (**b**) are present, along with secondary CL-bright features such as a convolute-CL rim (**c**) and smaller cross-cutting features (**d**). In comparison, crystal BM2 is CL-dark, and the panchromatic CL image was only obtained after overexposure, resulting in the identification of subtle patchy CL microstructures (**e**), (**f**). The hyperspectral CL map shows embayed CL-dark cores (**g**), (**h**), (**i**), a dark blue embayed core (**j**), and a subtle red-pink core (**k**). The remainder of the crystal displays very weak oscillatory zoning (**l**), overprinted by a CL-bright rim (**m**) and small cross-cutting features (**n**). Laser ablation pits (23 μm in diameter) are visible in the hyperspectral maps (**o**), (**p**). In BM2, inclusions of fluorite (**Fl**) and columbite group minerals (**CGM**) are visible as bright spots in the panchromatic CL image, but not in the hyperspectral CL map. The white corners denote the X-ray element map areas.

Figure 9. X-ray maps for cassiterite crystal BM1 from the Buriti mine. A cross cutting feature shows relative enrichment in Ti (**a**), but depletion in Nb (**b**) relative to concentration in primary growth structures. No relative change is seen in W (**c**) or Fe (**d**), however the concentration of

1054 these elements is at or below the detection limit in most of the crystal. Primary concentric growth
1055 zones are seen in Ti (**e**) and Nb (**f**). Zirconium is just above the detection limit in this crystal, and
1056 displays concentric growth zonation (**g**), and relative depletion in the cross-cutting structure (**h**).
1057 The cross-cutting structure also hosts inclusions of Fe-oxides (**i**).

1058 **Figure 10.** X-ray maps for cassiterite crystal BM2 from the Buriti mine. Tungsten enriched
1059 embayed cores (**a**), (**b**), (**c**), and a Nb enriched core (**d**), show corresponding Fe enrichment (**e**),
1060 (**f**), (**g**), (**h**). A core with a lower Nb enrichment (**i**) shows no Fe association, but a corresponding
1061 enrichment in Ti instead (**j**). The CL-bright rim (**k**) and the small cross-cutting features (**l**) are
1062 associated with moderate Ti concentrations. See text for further discussion.

1063 **Figure 11.** Cathodoluminescence imaging of a cassiterite crystal from White Lode, comparing
1064 panchromatic (**left**) with hyperspectral imaging (**right**). The hyperspectral maps have been
1065 colored with blue assigned to 200-500 nm, green to 500-600 nm and red to 600-900 nm. Crystal
1066 WL1 is CL dark, and the panchromatic CL image was only obtained via overexposure by
1067 changing the brightness and contrast settings to maximum. Under these conditions, small linear
1068 CL-bright cross-cutting features (**a**) and subtle mottled patches (**b**) are visible. In the
1069 hyperspectral CL map, further detail is illuminated with more CL-bright cross cutting features (**c**)
1070 and mottled-CL regions (**d**) not visible in the panchromatic image. The rest of the crystal remains
1071 CL-dark (**e**), (**f**). Near the rim of the crystal, a CL-bright cross-cutting feature (**g**) overlaps a
1072 mottled-CL region. Quartz inclusions (**Qz**), annotated on the panchromatic image, appear red in
1073 the hyperspectral map. The white corners denote the X-ray element map area.

1074 **Figure 12.** X-ray element maps for crystal WL1 from White Lode. Two chemically distinct
1075 regions are present, a region of high Sn purity (>32.5 at% Sn, yellow to orange regions, such as

around the region labelled **A**) and a region of low Sn purity (<32.5 at% Sn, blue to green regions, such as around the region labelled **B**). CL-bright cross-cutting features (e.g., from Figure 11c) and the mottled-CL features (e.g., from Figure 11d) are associated with the high Sn-purity region A (**c**, **d**) and show a depletion in Ti (**e**, **f**), Fe (**g**, **h**), Nb (**i**, **j**) and Ta (**k**, **l**) relative to the primary growth structures visible in region B. However, a part of region A with similar chemical characteristics to the cross-cutting CL features (**m**) does not display a CL-signature (see Figure 11f).

Figure 13. Paragenetic interpretation sketch for crystal WL1 from White Lode. The blue areas (**a**) correspond to regions of low SnO_2 purity due to substitution with Fe, Nb and Ta, and is interpreted to be primary. The purple regions (**b**) mark the areas of convolute CL identified through hyperspectral CL mapping (Figure 11), which are interpreted as secondary. This overlies the orange regions (**c**), which denote areas of high SnO_2 purity as identified from the Sn X-ray element maps (Figure 12) but show no CL signature. Part of this region appears euhedral (**d**), see text for further discussion. Inclusions are highlighted in grey, and brittle CL-bright cross cutting fractures are delineated with black lines.

Figure 1

Mount Bischoff

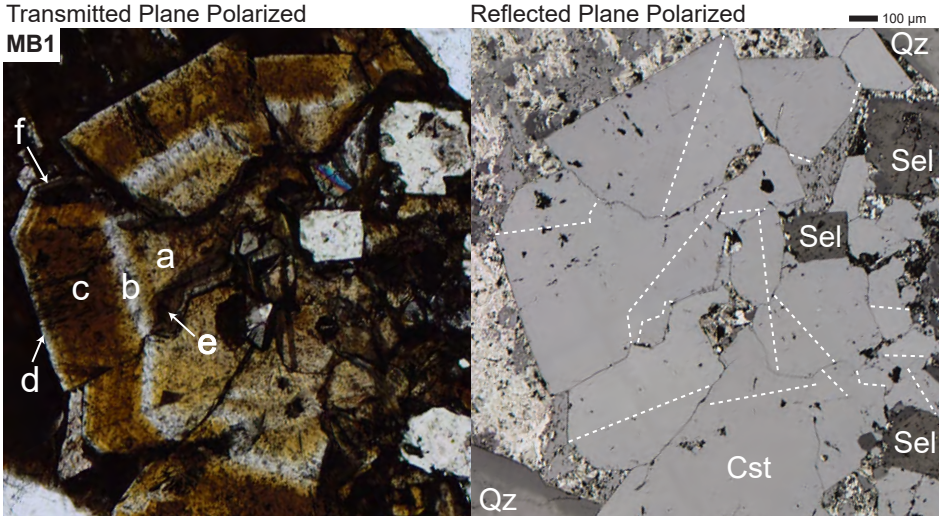

Figure 2

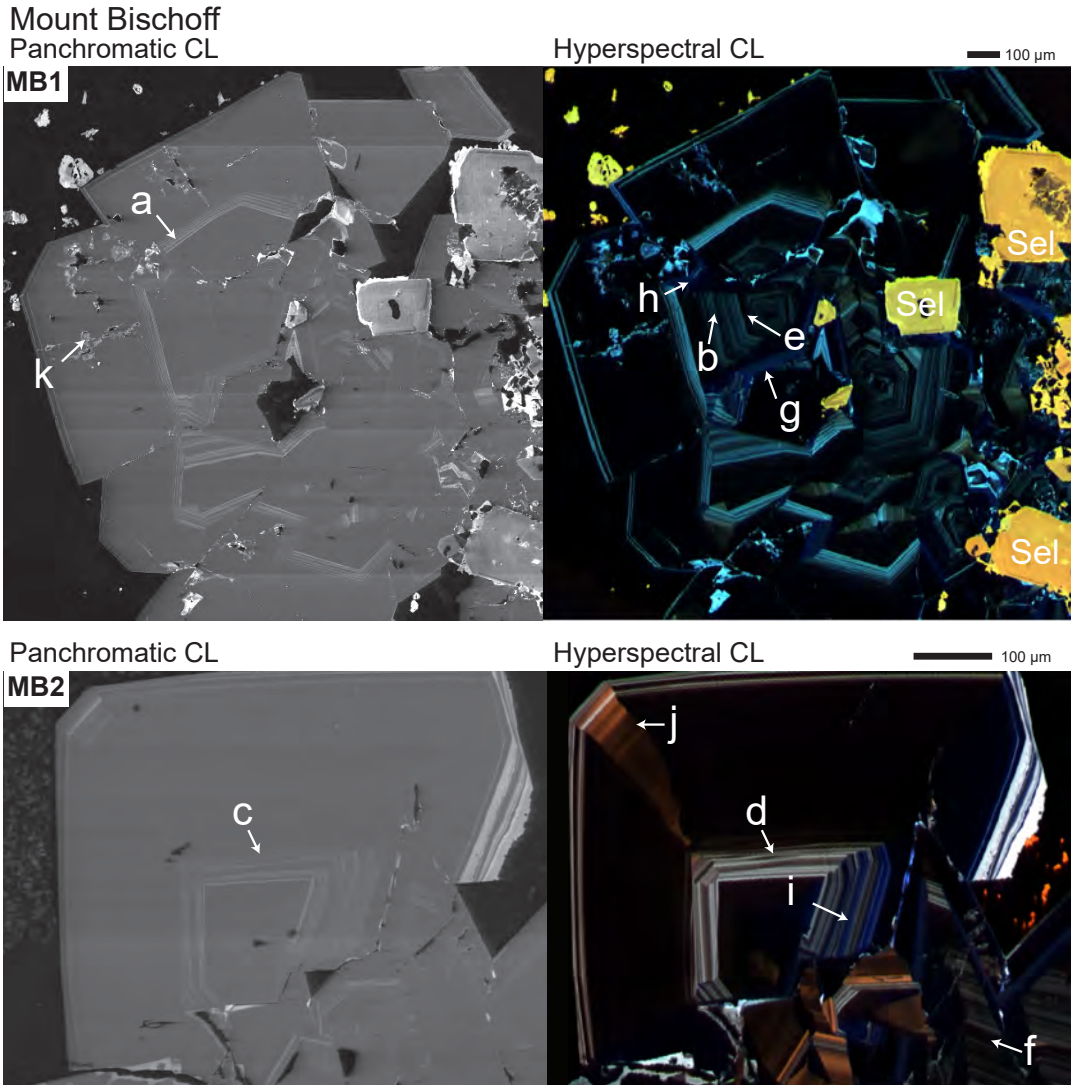
Mount Bischoff
Panchromatic CL
Hyperspectral CL
100 µm
MB1
a
k
h
b
e
g
Sel
Sel
Sel
Panchromatic CL
Hyperspectral CL
100 µm
MB2
c
j
d
i
f

Figure 3

Mount Bischoff - MB1

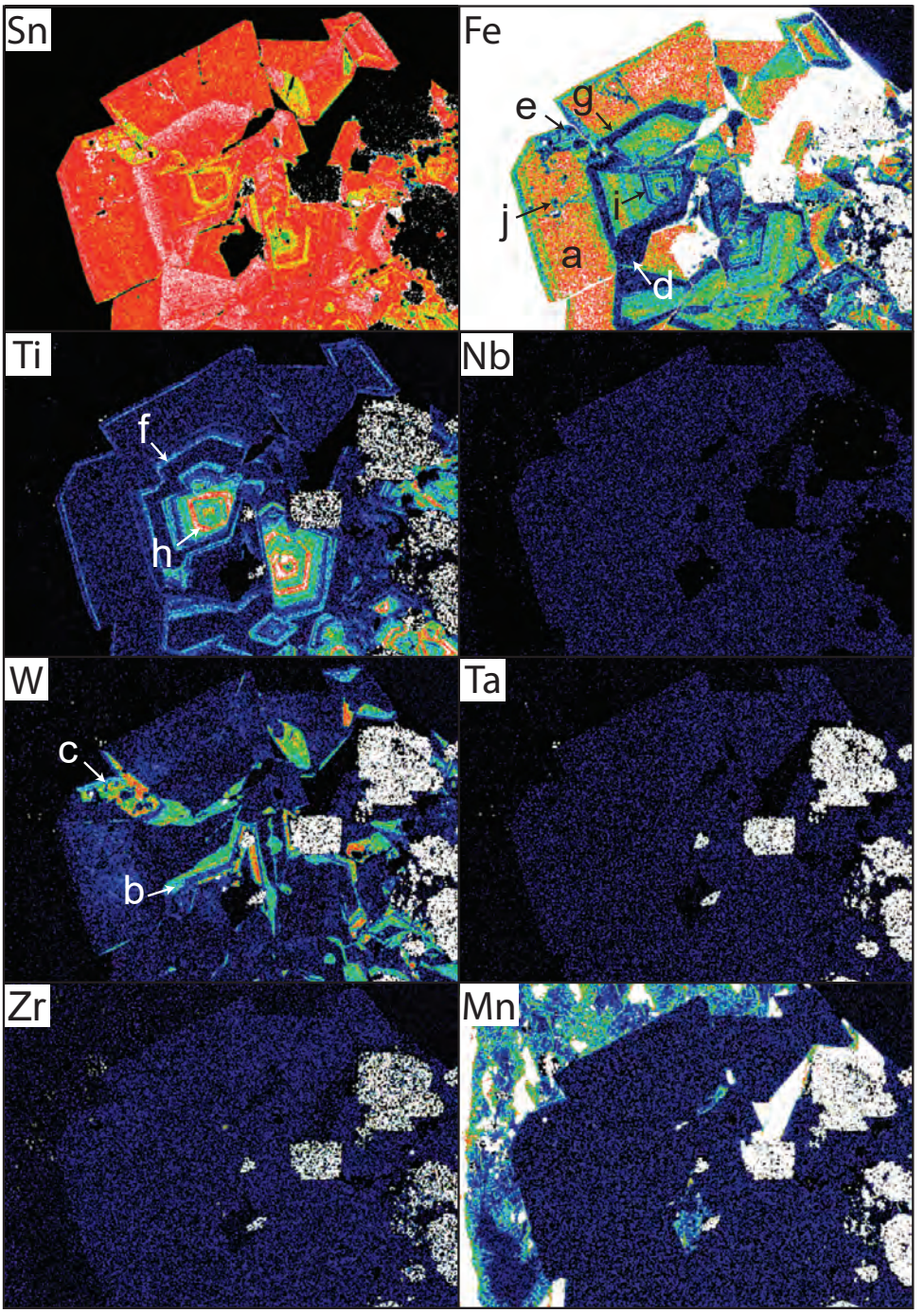

Figure 4

Mount Bischoff - MB2

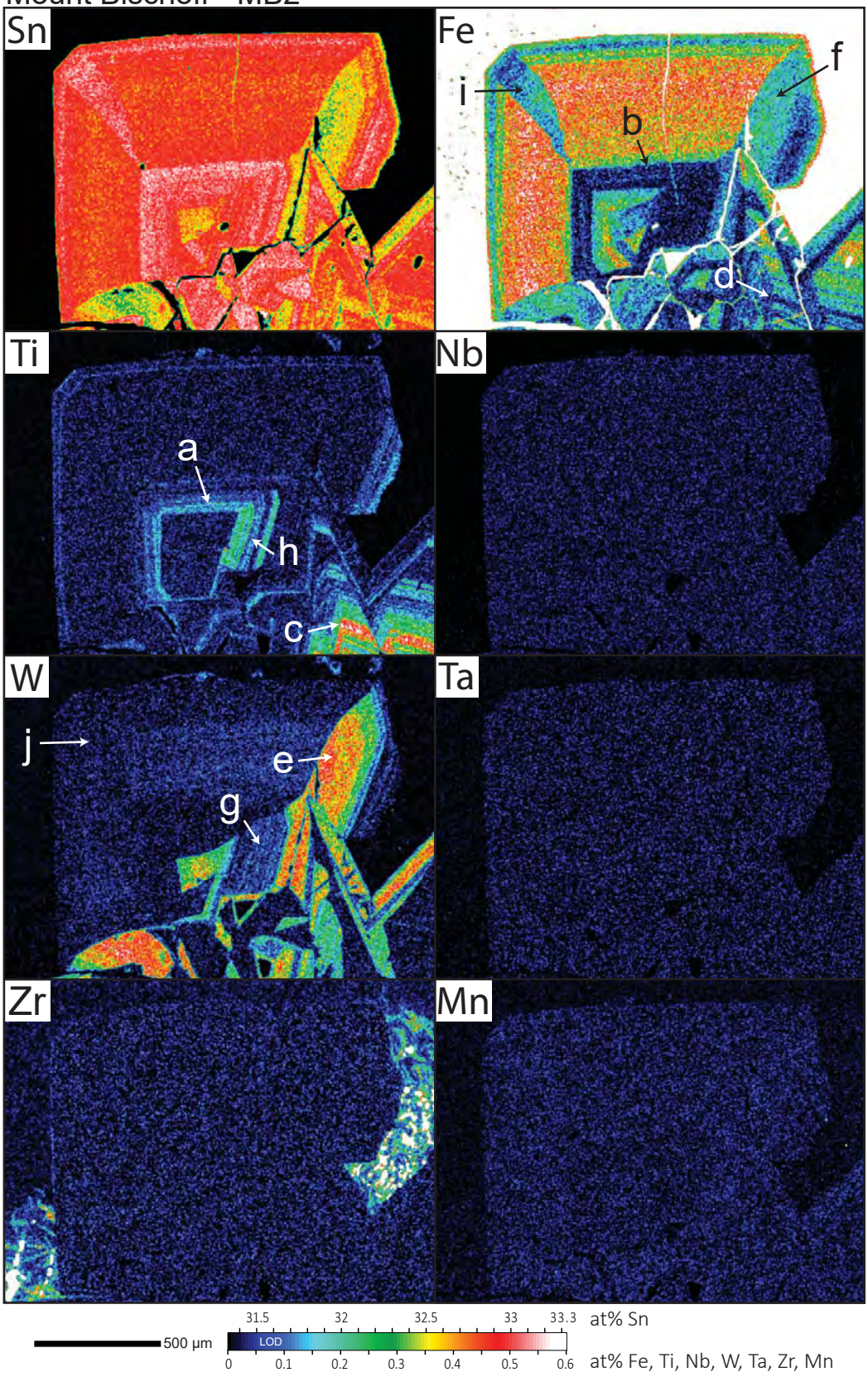

Figure 5

Saltwater Creek

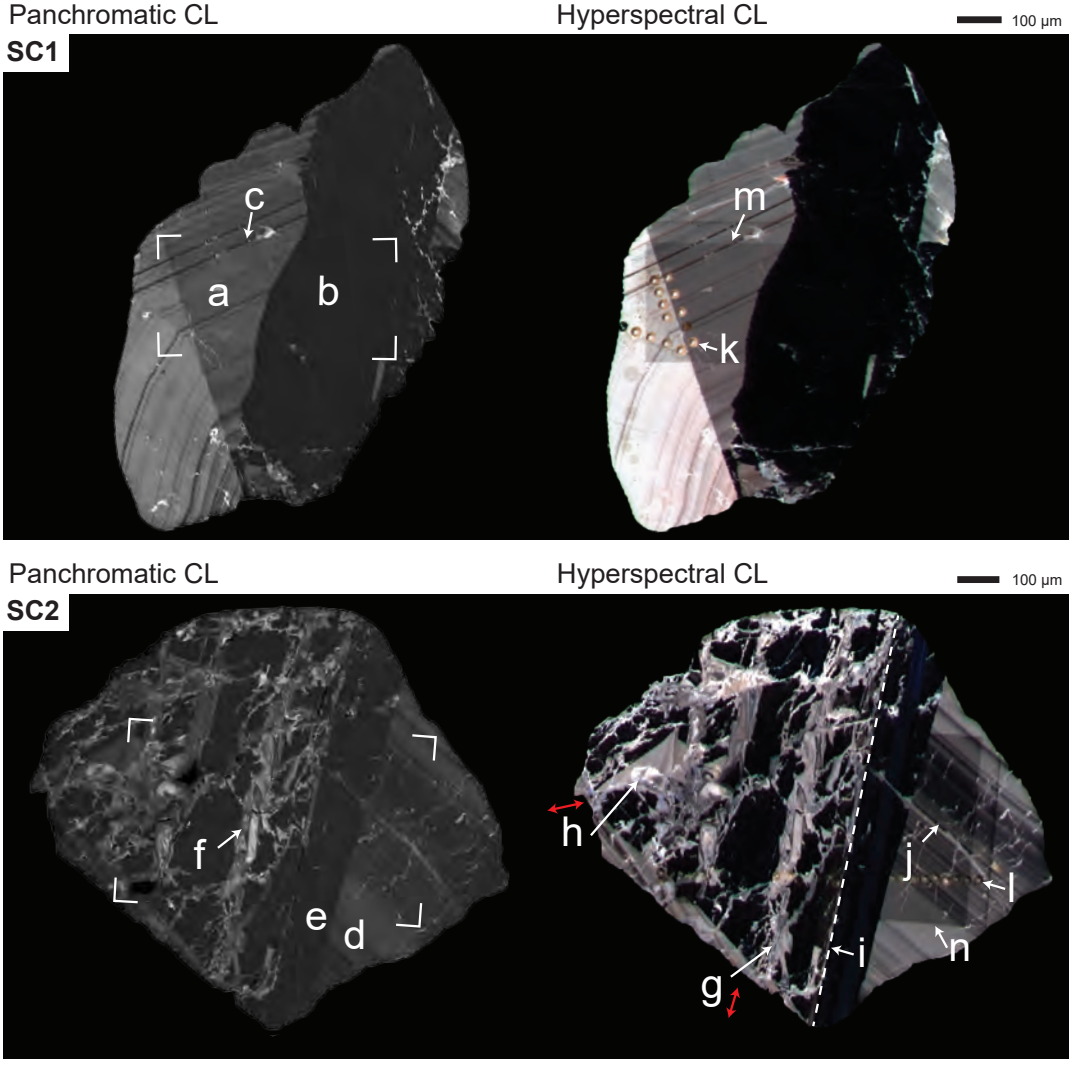

Figure 6

Saltwater Creek - SC1

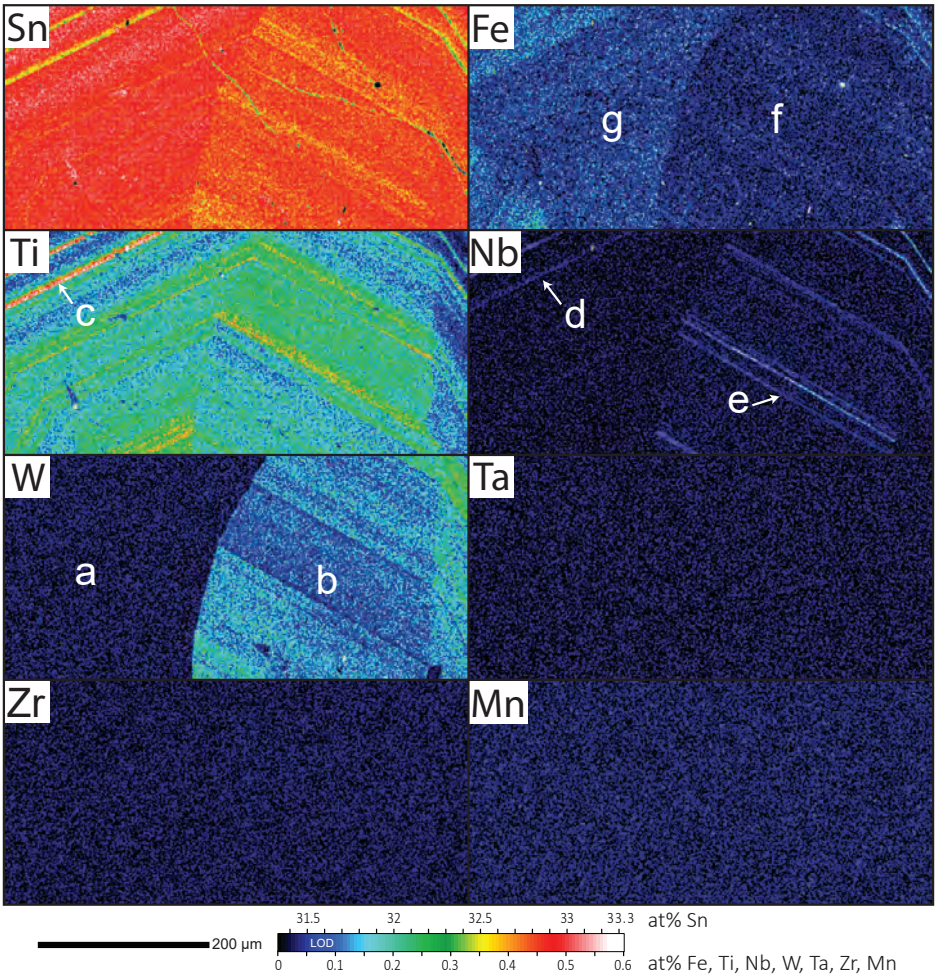

Figure 7

Saltwater Creek - SC2

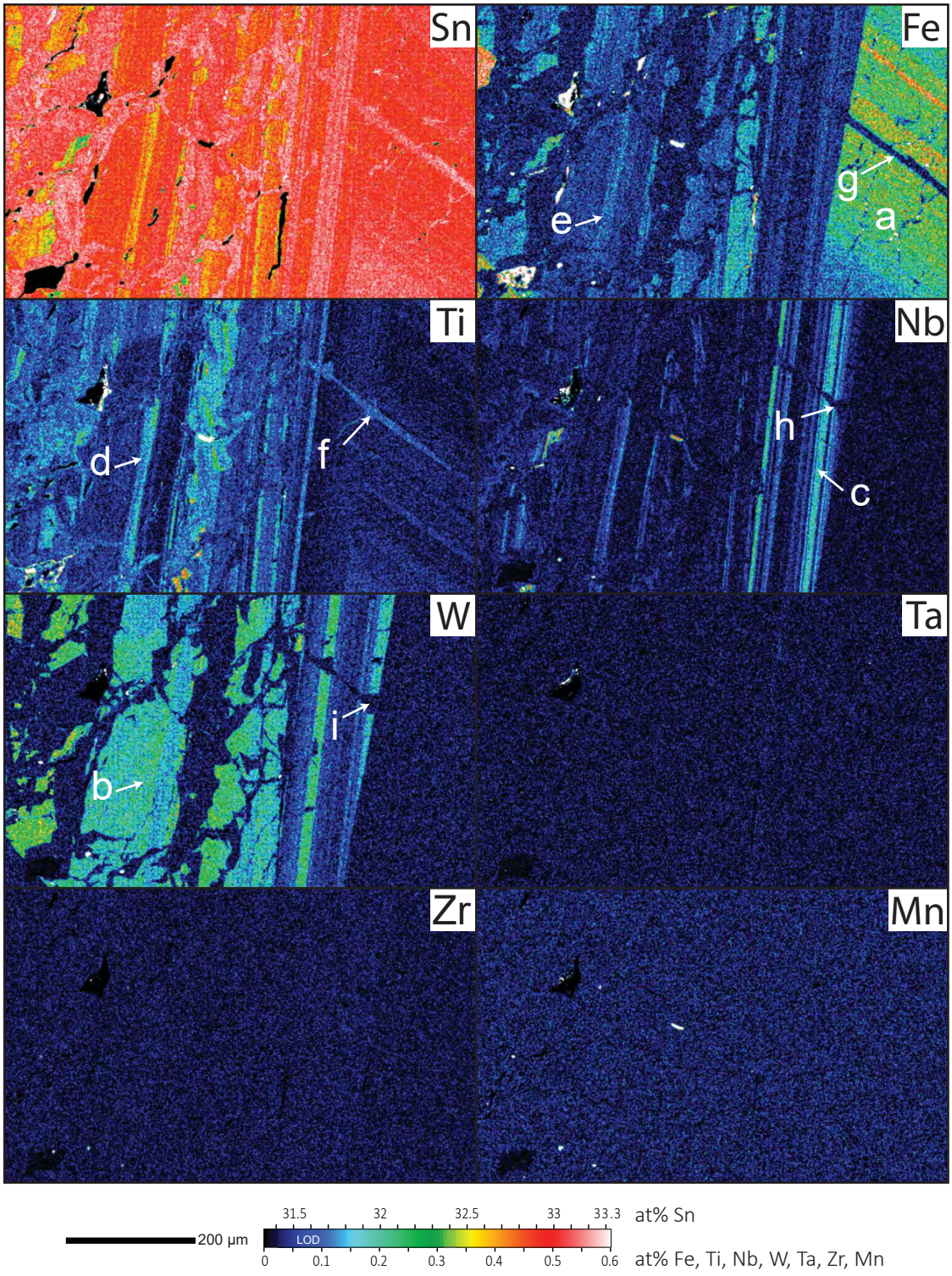

Figure 8

Buriti Mine

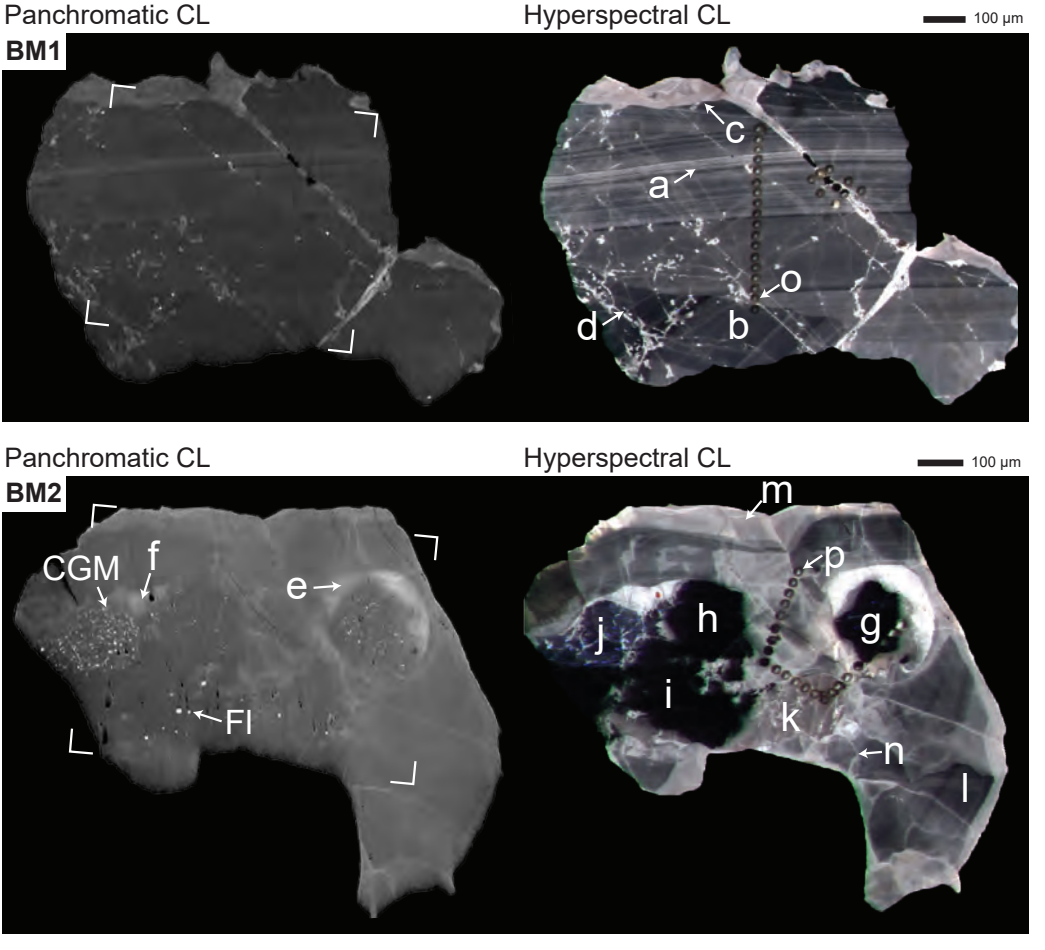

Figure 9

Buriti - BM1

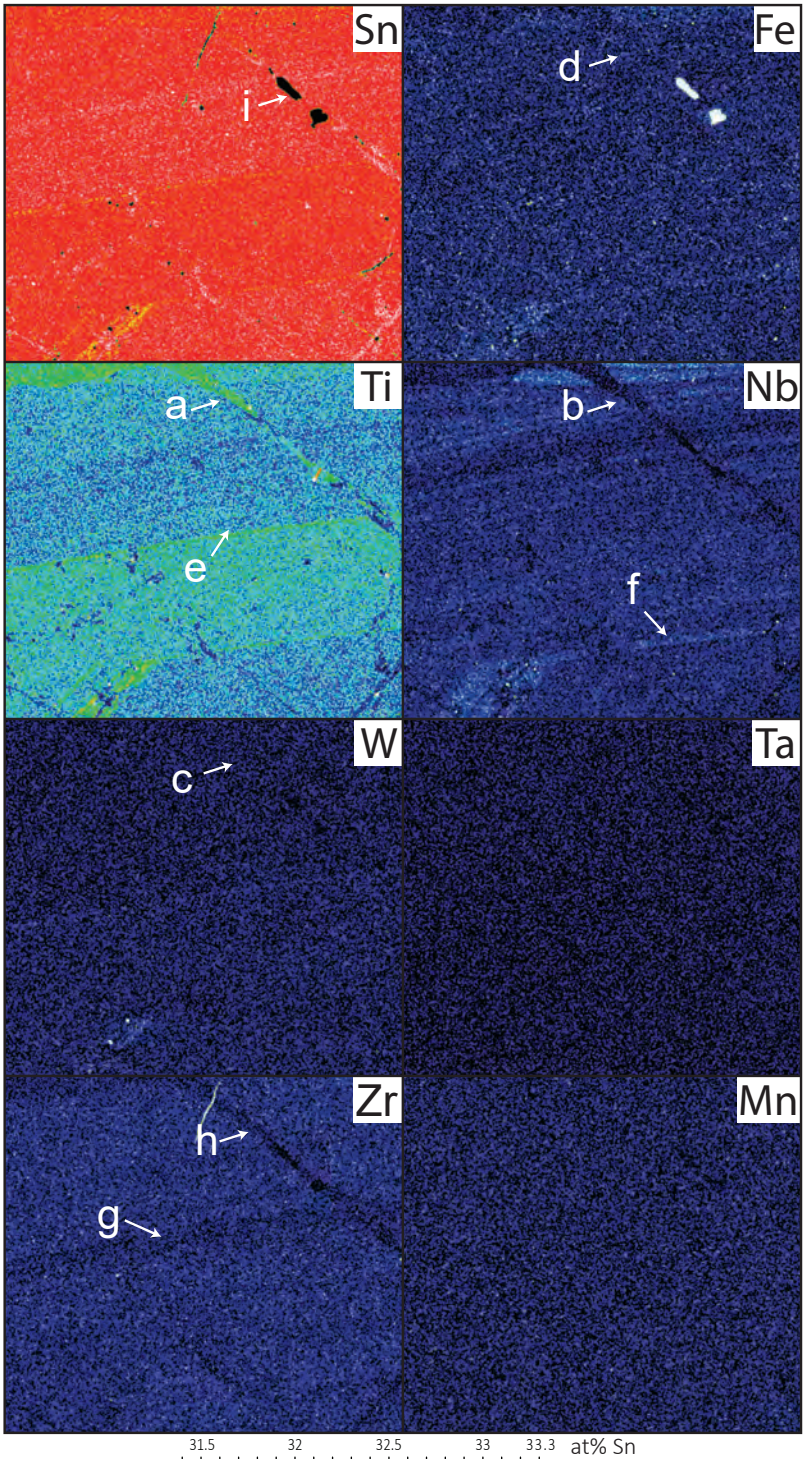

Figure 10

Buriti - BM2

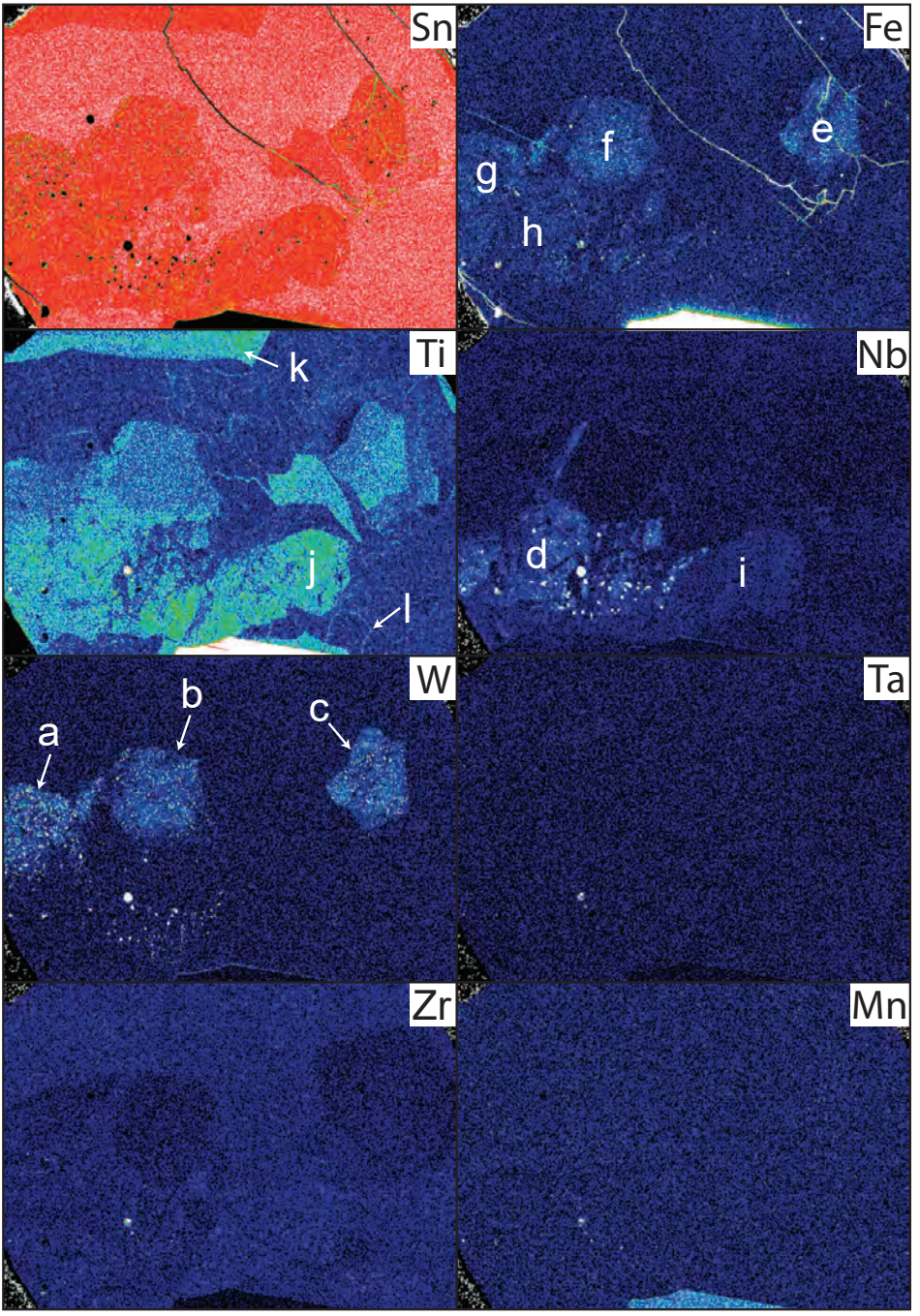

Figure 11

White Lode

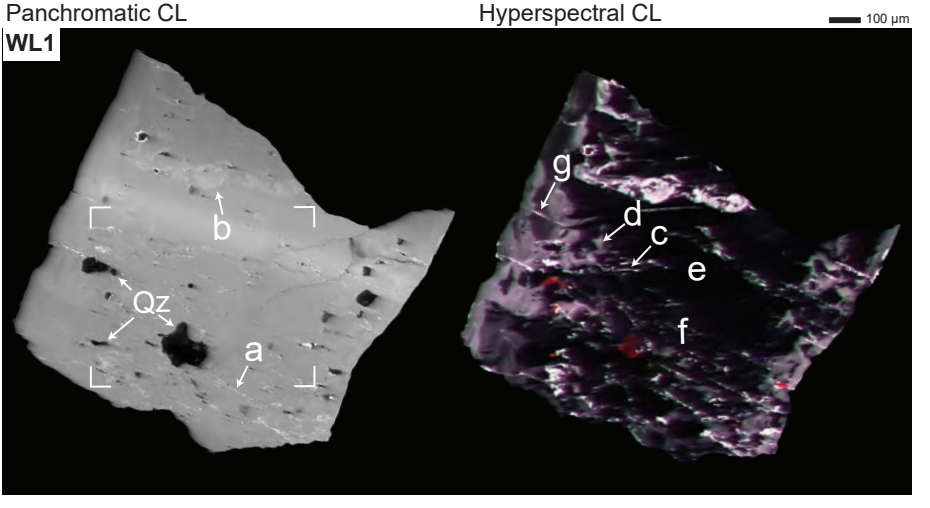

Figure 12

White Lode - WL1

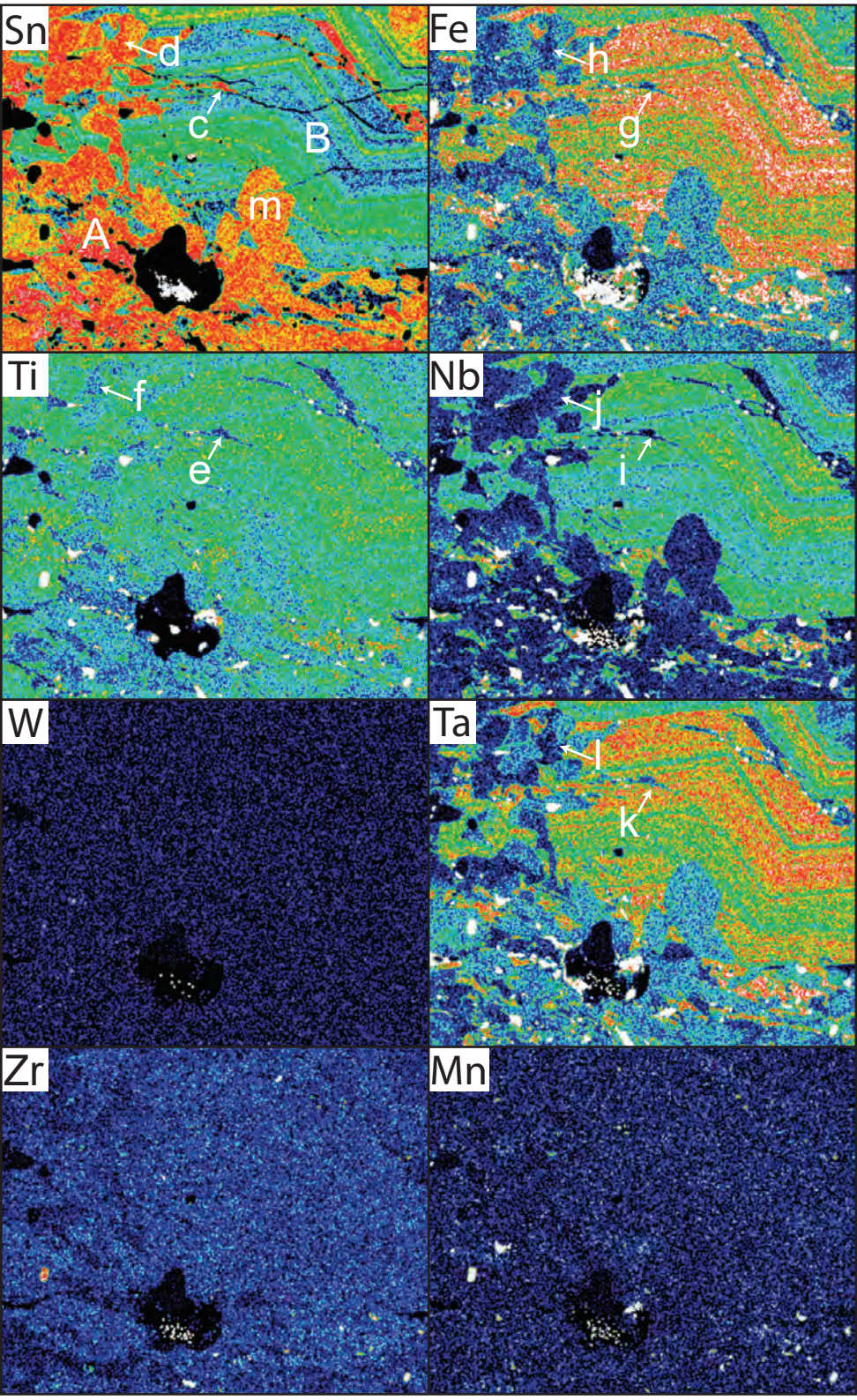

Figure 13

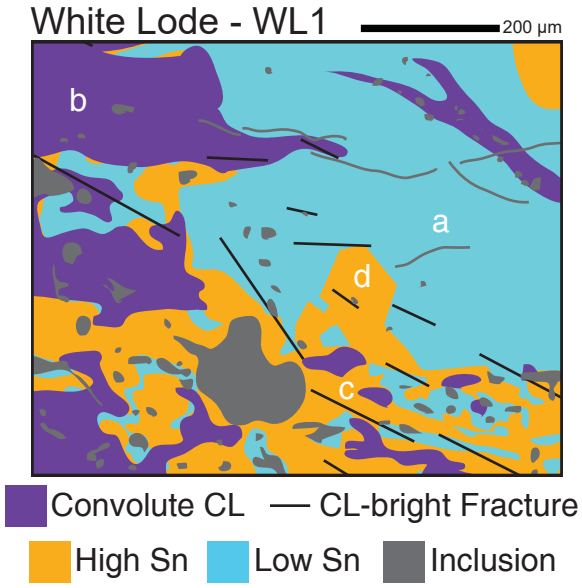
White Lode - WL1
200 µm
b
a
d
c
Convolute CL
CL-bright Fracture
High Sn
Low Sn
Inclusion